Modelling circulation, impulse and kinetic energy of starting jets with non-zero radial velocity

Michael Krieg[1,3] **and Kamran Mohseni**[1,2,3],†

[1]Department of Mechanical and Aerospace Engineering, University of Florida, Gainesville, FL 32611, USA

[2]Department of Electrical and Computer Engineering, University of Florida, Gainesville, FL 32611, USA

[3]Institute for Networked Autonomous Systems, University of Florida, Gainesville, FL 32611, USA

The evolution of starting jet circulation, impulse and kinetic energy are derived in terms of kinematics at the entrance boundary of a semi-infinite axisymmetric domain. This analysis is not limited to the case of parallel jet flows; and the effect of non-zero radial velocity is specifically identified. The pressure distribution along the entrance boundary is also derived as it is required for kinetic energy modelling. This is done without reliance on an approximated potential function (i.e. translating flat plate), making it a powerful analytical tool for any axisymmetric jet flow. The pressure model indicates that a non-zero radial velocity is required for any 'over-pressure' at the nozzle exit. Jet flows are created from multiple nozzle configurations to validate this model. The jet is illuminated in cross-section, and velocity and vorticity fields are determined using digital particle image velocimetry (DPIV) techniques and circulation, impulse and kinetic energy of the jet are calculated from the DPIV data. A non-zero radial velocity at the entrance boundary has a drastic effect on the final jet. Experimental data showed that a specific configuration resulting in a jet with a converging radial velocity, with a magnitude close to 40 % of the axial velocity at its maximum, attains a final circulation which is 90–100 % larger than a parallel starting jet with identical volume flux and nozzle diameter, depending on the stroke ratio. The converging jet also attains a final impulse which is 70–75 % larger than the equivalent parallel jet and a final kinetic energy 105–135 % larger.

Key words: jets, vortex flows, wakes/jets

1. Introduction

The study of short duration starting jets is almost synonymous with the study of vortex ring formation dynamics. In this type of flow a jet of fluid is expelled into a semi-infinite resting reservoir of similarly dense fluid, where the unstable shear layer/tube begins to spiral and the jet rolls into a single vortex ring or a vortex

† Current address: University of Florida, PO Box 116250, Gainesville, FL 32611, USA.
Email address for correspondence: mohseni@ufl.edu

ring with a trailing wake depending on the exact jetting parameters (Gharib, Rambod & Shariff 1998). The formation and evolution of vortex rings have been studied extensively by the fluid dynamics community; for a more in depth review of vortex rings, see Shariff & Leonard (1992). However, the formation analysis has been limited to a fairly restricted set of boundary flow conditions.

In practice, starting jets which enter a domain with nearly parallel axial streamlines can be created by ejecting the jet through a nozzle which consists of a long cylindrical tube. Here, as a point of clarification, we define 'nozzle' to be any solid structure which separates the emerging jet flow from the surrounding fluid reservoir. Commonly, flows ejected through a tube nozzle are driven by a moving piston internal to the cylinder. Starting flows with converging streamlines can be created by ejecting the jet through a converging conical nozzle. Converging conical nozzles are a family of nozzles extending from a nearly cylindrical tube to nozzles with increasing slope until the nozzle cone becomes a flat plate with a central circular orifice, which we will call an orifice nozzle. In these flows the fluid behind the nozzle must converge to pass through the central opening and these converging streamlines persist downstream of the nozzle exit plane. Similarly, starting flows with diverging streamlines can be created by diverging conical nozzles with the maximum divergence created by an unbounded source just outside the domain. It should be noted here that during the early stages of vortex formation the vortex ring is very close to the entrance boundary, and will induce a radial velocity on the flow crossing the entrance plane. However, throughout this paper we will refer to jet flows which are expelled through tube nozzles as parallel jets, and jet flows expelled through converging or diverging nozzles as non-parallel in reference to the nature of the source flow, despite the influence of the vortex ring at early formation times.

Experimental studies on parallel starting jets have characterized jet velocity profiles and vortex ring geometries (Didden 1979). Gharib *et al.* (1998) used digital particle image velocimetry (DPIV) to get the full velocity field of parallel flows and used that data to determine vortex ring circulation and vortex ring separation dynamics. Using numerical simulations this analysis was extended to flows with a much larger range of jet velocity profiles (Rosenfeld, Rambod & Gharib 1998) and shear layer growth/acceleration (Mohseni, Ran & Colonius 2001). The circulation of the primary vortex ring is usually modelled by a one-dimensional (1D) slug model (Glezer 1988; Shariff & Leonard 1992; Gharib *et al.* 1998; Mohseni & Gharib 1998) (a more in depth description is given in §6) or through the self-similar roll-up of the vortex tube extending from the nozzle (Pullin 1978; Saffman 1978; Pullin 1979; Pullin & Phillips 1981; Nitsche & Krasny 1994). The circulation and impulse of the jet were modelled by the 1D slug model with an added contribution due to 'over-pressure' by Krueger & Gharib (2003) and Krueger (2005). However, vortex rings formed from non-parallel starting jets have been minimally studied even though non-parallel starting jets exist in several vortex flows from squid and jellyfish propulsion, to cardiac flows, to synthetic jet actuation. The importance of the axial gradient of radial velocity, $\partial v/\partial x$, to the generation of circulation was noted by Didden (1979), who also observed substantial radial velocity during the initial phases of vortex ring formation. Krueger (2005) derived an analytical model for the circulation generated in starting jets ejected from both tube and orifice nozzles, where the effect of the radial velocity gradient on over-pressure is emphasized. This model was validated by numerical simulations in Krueger (2008) showing nearly double the circulation in jets generated through orifice nozzles over tube nozzles with equivalent piston velocity programs, nozzle diameters, and stroke ratios, which was well predicted by the analytical model for large stroke ratio
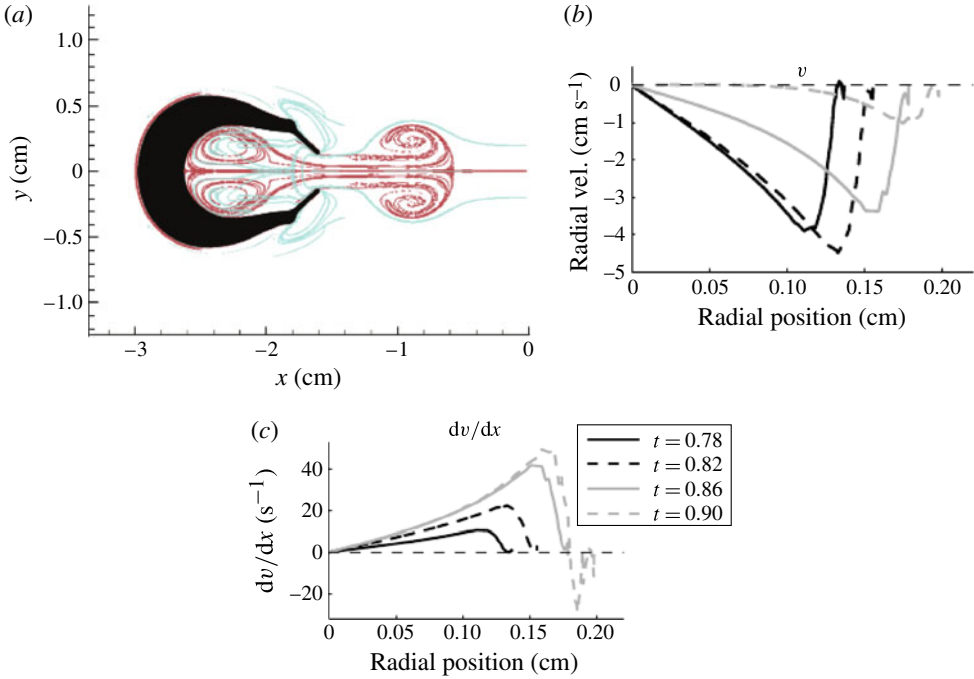
FIGURE 1. (Colour online) A swimming jellyfish, *Sarsia tubulosa*, is shown along with stable (blue) and unstable (red) LCSs around the body for a given instant during the jetting phase (*a*). Local radial velocity at the velar opening is plotted for several instances in (*b*), as well as the gradient of the radial velocity (*c*). (Data reproduced from Sahin, Mohseni & Colins (2009) and Lipinski & Mohseni (2009*b*).)

jets. Rosenfeld, Katija & Dabiri (2009) investigated the effect the added radial velocity had on the circulation of the forming jet, through numerical simulations utilizing a range of converging conical nozzles. This paper provides additional empirical data to support these findings and presents an analytical model for circulation, impulse, energy and nozzle pressure which only requires knowledge of the velocity profiles at the entrance boundary (nozzle exit plane). These velocity profiles are also parameterized here for multiple nozzle configurations.

  Non-parallel starting jets serve an important function in the locomotion of marine animals such as jellyfish and squid. Jellyfish locomotion presents an interesting optimization problem, because there are multiple competing objectives involved with jetting. Lipinski & Mohseni (2009*a,b*) demonstrated that the jetting process is used for feeding as well as locomotion using Lagrangian coherent structure (LCS) analysis (for a summary of LCS analysis refer to Haller & Yuan (2000) and Shadden, Lekien & Marsden (2005)). The Froude propulsive efficiency of multiple species of jellyfish were examined by Sahin & Mohseni (2008, 2009) and Sahin *et al.* (2009) and empirical DPIV measurements by Dabiri *et al.* (2010) show similar efficiency characteristics for several different species. However, it is still not clear exactly which swimming behaviours benefit propulsion versus feeding and respiration. Figure 1(*a*) shows stable and unstable material transport barriers (LCS) around a swimming jellyfish taken from simulations in Sahin *et al.* (2009) and Lipinski & Mohseni (2009*b*); where the velar opening can clearly be seen to be a converging conical nozzle

and figure 1(*b*) shows the converging radial velocity of the expelled jet. Therefore, the analytical tools of this paper can be used to analyse the jellyfish jet, which in turn will help to clarify the genetic optimization, since impulse and kinetic energy of the jet are directly related to propulsion and efficiency, whereas creating a jet with increased circulation may be tied to other functions such as feeding or respiration. Squid locomotion has also been linked to vortex ring formation dynamics in the propulsive jet (Anderson & Grosenbaugh 2005; Bartol *et al.* 2008, 2009), and again simplified parallel flows do not exactly mimic the jetting seen in squid. The squid funnel changes shape during pulsation and can exhibit characteristics of both tube nozzles and converging conical nozzles. A converging radial velocity can be seen very close to the exit of the funnel in figure 8 of Anderson & Grosenbaugh (2005), which shows the velocity field of the jet produced from a swimming adult squid. Vortex ring formation in the left ventricle has been tied to cardiac performance by Gharib *et al.* (2006), and again heart valves at times behave like converging conical nozzles, which should be taken into account when considering formation dynamics.

An accurate model for determining the kinetic energy of a fluid jet as well as the pressure along the jet entrance boundary is an invaluable tool for analysing any jet propulsor, such as those examined by Mohseni (2006). Propulsive efficiency of a vehicle driving mechanism is inversely proportional to the energy required to generate motion. For propulsors in a fluid environment this is directly related to the kinetic energy of the jet created while propelling the vehicle forward. The pressure at the entrance boundary of a parallel starting jet was predicted by Krueger (2005) by equating the starting jet flow to the flow around a translating flat plate and determining pressure from the resulting potential function. The modelling of this paper allows jet energy and nozzle pressure to be determined using only the velocity profiles at the jet entrance/nozzle exit boundary. Although we focus mainly on finite jets in this paper, the analysis can be extended to continuous jets as well.

The rate of circulation and momentum transferred to the external flow plays a key role in defining synthetic jet formation criteria. Characteristic jet flow parameters such as the Strouhal number are determined entirely from axial jet velocity; however, as is shown in this paper, the radial velocity of the jet has a significant affect on the rate of circulation, impulse and energy added to the external flow. Holman *et al.* (2005) approximated the vorticity flux from axial jet velocity which was related to the Strouhal number to give a criterion for synthetic jet formation. The entrance geometry of the synthetic jet nozzle was observed to strongly affect this criterion and a heuristic expression was used to modify the vorticity flux based on nozzle entrance curvature. Similarly, the entrance length was characterized for zero-net mass-flux devices with a variety of channel entrance conditions by Raju *et al.* (2005), showing that a sharp edge at the channel entrance has a strong effect on vorticity flux and entrance length. While not pursued here, we expect that if the characteristic vorticity flux and Strouhal number are redefined to include contributions from radial velocity, the jet formation constant and entrance length would converge upon a more universal value independent of specific device geometry. In addition, predicting jet kinetic energy and nozzle pressure could serve as a powerful tool for analysing and designing synthetic jet actuators. One particular application would be improving energetic cost functions for optimization of synthetic jet flow control for aerofoil drag reduction.

A more complete model for the circulation, impulse and energy of a jet formed from incoming flow with non-zero radial velocity is given based on the flux of kinematic quantities across the entrance plane. The pressure profile at the entrance boundary which is required to evaluate energy is also derived in terms of the entrance
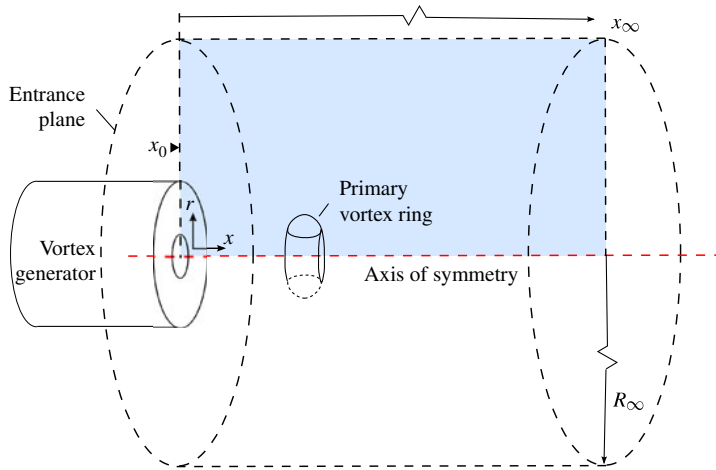
FIGURE 2. (Colour online) Definition of problem coordinate system and control volume boundaries.

kinematics. The velocity profiles at the inflow are then parameterized for a set of nozzle configurations allowing the invariants of motion to be calculated from a limited number of parameters. It should be noted that the hydrodynamic impulse is modelled, because the net hydrodynamic impulse of the jet after pulsation is equal to the integral of the net external force required to create the flow. This is not in all cases equal to the total fluid momentum, as will be discussed in this paper. The derivation of total jet circulation, impulse and kinetic energy is given in § 2, and § 6 provides a general form for the axial and radial velocity profiles observed in several experimental nozzle flows. A description of the vortex generator is given in § 3, and § 4 illustrates the experimental apparatus used to capture jet flow dynamics. The velocity and vorticity field of the axisymmetric flow is determined through DPIV as described in § 5. Section 7 describes the experimentally observed differences between parallel and non-parallel starting jets as well as the accuracy of models presented in § 2 for predicting circulation, impulse and energy.

2. Modelling the jet

The circulation, hydrodynamic impulse and kinetic energy of a starting jet are modelled with a control volume analysis which relates the rate of change of those quantities to the kinematics at the volume boundary. The fluid in the control volume is assumed to start at rest, so that integration of these rates over time gives the total circulation, impulse and energy of the jet. This section will present the control volume analysis in terms of unspecified velocity profiles at the entrance boundary. These velocity profiles are specific to the method used to generate the flow and will be parameterized for several actuation methods in § 6.

We consider a semi-infinite axisymmetric control volume, so that the position of any point in this volume can be described by the cylindrical coordinates r, ϕ and x. The control volume extends from the axis of symmetry to infinity, R_∞, in the radial direction and from the source of the starting flow, x_0, to infinity, x_∞, in the axial direction as is depicted in figure 2. The velocity vector in the cylindrical coordinate system is $\boldsymbol{u} = [v, w, u]^{\mathrm{T}}$. The model presented in this section will presume that the

control volume is truly infinite in the directions specified, when in actuality the experimental fluid reservoir is bounded by the walls of the testing tank. However, the distances to these boundaries are sufficiently large to consider the fluid reservoir unbounded, R_∞ is at least 50 times the nozzle radius and x_∞ is at least 140 times the nozzle radius.

The flow is assumed to be incompressible with a constant density, ρ. The flow is also assumed to be symmetric about the x-axis with no swirl, so that $w = 0$ and $\partial/\partial\phi = 0$. Therefore, the continuity equation can be written

$$\frac{\partial u}{\partial x} + \frac{\partial v}{\partial r} + \frac{v}{r} = 0. \tag{2.1}$$

The walls of the tank and the centre of mass of the fluid remain stationary meaning that there is no net force acting on the control volume and forces are transmitted between the fluid and the tank walls through pressure forces. There are no additional non-conservative forces acting on the fluid. It is also assumed that the effect of viscous dissipation is negligible and the governing dynamics of the flow field are modelled by the momentum equation,

$$\frac{\mathrm{D}\boldsymbol{u}}{\mathrm{D}t} = -\frac{1}{\rho}\boldsymbol{\nabla}P. \tag{2.2}$$

Here P is the gauge pressure or local pressure combined with the potentials of conservative forces, including gravity. Using numerical simulations Mohseni *et al.* (2001) showed that the normalized circulation and energy of starting jets created with Reynolds number above 2000 (ranging up to 7300) attained consistent values, indicating a sufficiently thin shear layer. Therefore, the inviscid approximation should be valid for jets with $Re \geqslant 2000$. The simulations of Mohseni *et al.* (2001) utilized non-conservative forcing rather than physical nozzle boundaries in the vortex generation process; however, the viscous interaction with the nozzle boundaries results in the velocity profiles which are the boundary conditions of this control volume analysis, so the fluid viscosity is only considered negligible as the jet evolves downstream. In fact, the fluid viscosity is required to predict axial velocity profiles as described in § 6.1.2. Taking the curl of the momentum equation, one obtains the vorticity transport equation,

$$\frac{\partial\boldsymbol{\omega}}{\partial t} = \boldsymbol{\nabla} \times (\boldsymbol{u} \times \boldsymbol{\omega}). \tag{2.3}$$

In an axisymmetric domain with no swirl the vorticity only exists in the $\hat{\phi}$ direction meaning that, $\omega = \partial v/\partial x - \partial u/\partial r$.

2.1. *Circulation*

The total circulation of the jet is just the integral of the vorticity over the axisymmetric plane, $[r, x]$. For inviscid fluids, circulation is an invariant, and the rate of change of circulation is equal to the flux of vorticity into the control volume. Since the vorticity is confined to the core of the primary vortex ring and trailing shear layer, the flux of vorticity across the boundaries $r = R_\infty$ and $x = x_\infty$ drops to zero, and the rate of change of the circulation is equal to the flux of vorticity across the nozzle exit plane (Didden 1979),

$$\frac{\mathrm{d}\Gamma}{\mathrm{d}t} = \int_0^{R_\infty} u\left(\frac{\partial v}{\partial x} - \frac{\partial u}{\partial r}\right)\,\mathrm{d}r. \tag{2.4}$$

As was noted by Rosenfeld *et al.* (1998, 2009) the second term is independent of the specific axial velocity profile so that given the centreline velocity, u_0, the evolution of circulation becomes

$$\frac{\mathrm{d}\Gamma}{\mathrm{d}t} = \frac{1}{2}u_0^2 + \int_0^{R_\infty} u\frac{\partial v}{\partial x}\,\mathrm{d}r. \tag{2.5}$$

For parallel starting jets the rate of change of circulation is mostly dependent on the axial velocity at the centreline, but the additional term becomes significant for non-parallel starting jets.

2.2. *Hydrodynamic impulse and momentum*

Now we perform a similar derivation for the rate of change of impulse in terms of the same kinematic terms at the entrance boundary. The hydrodynamic impulse of the control volume is defined as

$$\boldsymbol{I}_h \equiv \frac{\rho}{2}\int_{CV} \boldsymbol{x}\times\boldsymbol{\omega}\,\mathrm{d}\boldsymbol{x}. \tag{2.6}$$

It was shown by Lamb (1945) (and in vector form by Saffman (1992)) that in an unbounded fluid with confined vortical region, the rate of change of the hydrodynamic impulse is equal to the total non-conservative body forces acting on the fluid. The following analysis gives the rate of change of the hydrodynamic impulse in a semi-infinite domain (more specifically the control volume of this section). As was mentioned in the introduction, starting jets are often used for underwater propulsion and instantaneous force exerted on the vortex generator is of critical importance. Therefore, it should be noted that the instantaneous force on the vortex generator is not exactly equal to the rate of impulse created in the jet (control volume shown in figure 2), since the control volume is bounded. There are forces exerted on the vortex generator associated with accelerating and decelerating the internal cavity fluid at the onset and termination of pulsation, respectively. Although these instantaneous forces are significant, they are in general cyclical and can be considered internal forces so that the integral of the net propulsive force is equal to the jet impulse, after pulsation, as calculated in this section.

Taking the total derivative of the hydrodynamic impulse and using the vorticity transport equation (2.3) as the rate of change of vorticity provides rate of change of hydrodynamic impulse of an axisymmetric inviscid jet with no swirl,

$$\frac{\mathrm{d}\boldsymbol{I}_h}{\mathrm{d}t} = \frac{\rho}{2}\begin{bmatrix} \iint -x\left(\dfrac{\partial(-u\omega)}{\partial x} - \dfrac{\partial(v\omega)}{\partial r}\right)2\pi r\,\mathrm{d}r\,\mathrm{d}x \\ 0 \\ \iint r\left(\dfrac{\partial(-u\omega)}{\partial x} - \dfrac{\partial(v\omega)}{\partial r}\right)2\pi r\,\mathrm{d}r\,\mathrm{d}x \end{bmatrix}. \tag{2.7}$$

The hydrodynamic impulse in the radial direction is of little concern (and indeed can be shown to be equal to zero), so we will focus on impulse in the axial direction. The volume integral can be simplified to a sum of surface integrals by taking a series of partial integrations and utilizing the incompressibility condition.

$$\frac{\mathrm{d}I_h}{\mathrm{d}t} = \rho\pi\int_0^{R_\infty} \left[-r^2u\omega + rv^2 - ru^2\right]_{x_0}^{x_\infty}\mathrm{d}r - \rho\pi\int_{x_0}^{x_\infty} \left[r^2v\omega + 2rvu\right]_0^{R_\infty}\mathrm{d}x. \tag{2.8}$$

The integral terms at the far-field boundary can be eliminated using an order of magnitude stream function analysis. The vorticity is confined to the core of the primary vortex ring and the trailing shear flow, so along the surfaces at infinity the bounded vorticity appears as a point vortex at the origin and the stream function can be treated like that in an unbounded spherical domain since the vorticity is an equally infinite distance from the boundaries in the radial and axial directions, respectively. The first integrand term in both integrals of (2.8) involve the vorticity which is known to be zero at the far-field boundaries. Using the Stokes stream function Cantwell (1986) and Saffman (1992) showed that in an unbounded spherical domain the velocities, u and v, scale with $\tilde{r}^{-2}$ ($\tilde{r}$ is the radial distance in the spherical domain $\tilde{r} = \sqrt{r^2 + x^2}$). From this relation, the remaining integrand terms of (2.8) at far-field boundaries scale with $\tilde{r}^{-3}$ meaning that the integrand drops to zero faster than the integration area grows at infinity. Therefore, the surface integrals taken along the boundaries $x = x_\infty$ and $r = R_\infty$ can be neglected and the surface integral of (2.8) need only be calculated along the boundary $x = x_0$.

$$\frac{\mathrm{d}I_h}{\mathrm{d}t} = \rho\pi \int_0^{R_\infty} \left[2u^2 r + u\frac{\mathrm{d}v}{\mathrm{d}x}r^2 - v^2 r \right]_{x=x_0} \mathrm{d}r. \tag{2.9}$$

The first term is the familiar flux of axial momentum across the entrance boundary. Several studies (Glezer 1988; Shariff & Leonard 1992; Gharib *et al.* 1998; Mohseni & Gharib 1998) approximate the jet circulation assuming that the jet leaves the vortex generator with a uniform axial velocity and no radial velocity (meaning that the jet is considered a uniform slug of fluid). Using the slug model approximation, the rate of change of hydrodynamic impulse can be simplified to $\mathrm{d}I_h = \pi u_p^2 R^2 \,\mathrm{d}t$. The integral of this term is used by Mohseni *et al.* (2001) and Krieg & Mohseni (2008) to predict the total impulse of the jet. For simplicity, throughout the remainder of the paper the hydrodynamic impulse in the axial direction will just be referred to as the impulse of the jet, I.

The total momentum of the control volume, $\boldsymbol{H} = \int \boldsymbol{u} \,\mathrm{d}\boldsymbol{x}$, is not in general equal to the hydrodynamic impulse. Classical analysis by Cantwell (1986) has shown that in a spherical control volume, extended to infinity, with vorticity localized to a confined central region the relationship is $H = 2I/3$. To illustrate this point we integrate the momentum equation (2.2) over the entire control volume to get the rate of change of the total momentum, $\boldsymbol{H}$, and making a partial integration gives only surface integral terms,

$$\rho \int \frac{\partial \boldsymbol{u}}{\partial t} \,\mathrm{d}\boldsymbol{x} = \frac{\mathrm{d}\boldsymbol{H}}{\mathrm{d}t} = -\rho \int \boldsymbol{u} \cdot \nabla \boldsymbol{u} \,\mathrm{d}\boldsymbol{x} - \int \nabla P \,\mathrm{d}\boldsymbol{x}$$
$$= -\rho \int \boldsymbol{u}\,(\boldsymbol{u} \cdot \boldsymbol{n}) \,\mathrm{d}S - \rho \int \boldsymbol{u}\,(\nabla \cdot \boldsymbol{u}) \,\mathrm{d}\boldsymbol{x} - \int P\boldsymbol{n} \,\mathrm{d}S$$
$$= -\rho \int \boldsymbol{u}\,(\boldsymbol{u} \cdot \boldsymbol{n}) \,\mathrm{d}S - \int P\boldsymbol{n} \,\mathrm{d}S. \tag{2.10}$$

Here $\boldsymbol{n}$ is the unit normal which points out of the surface by convention. Under the same boundary conditions as were used to simplify (2.8), the rate of change of the total momentum in the axial direction is

$$\frac{\mathrm{d}H_x}{\mathrm{d}t} = 2\rho\pi \int_0^{R_\infty} u^2 r \,\mathrm{d}r - 2\pi \int_0^{R_\infty} [P(x_\infty, r) - P(x_0, r)] \, r \,\mathrm{d}r. \tag{2.11}$$

The first integral is the flux of axial momentum, which is identical to the first term in (2.9). Krueger & Gharib (2003) define an added force measured during experimentation which they term the pressure impulse,

$$I_P(t) = \int_0^t \int_A [P(r, \tau) - P_\infty] \, \mathrm{d}S \, \mathrm{d}\tau, \qquad (2.12)$$

where A is the nozzle area and P_∞ is the stagnation pressure; $P_\infty = \lim_{x \to +\infty} P(x, 0)$. This term can readily be equated to the pressure term of (2.11), since the pressure can be assumed to be uniform at the boundary $x = x_\infty$.

One useful feature of the hydrodynamic impulse derivation (2.9) is that the nozzle pressure does not need to be taken into account.

2.3. *Kinetic energy*

The rate of change of kinetic energy of the system, $E = \int \rho \boldsymbol{u}^2 \, \mathrm{d}V/2$, is derived for an incompressible, inviscid control volume in multiple classic texts (Lamb 1945; Landau & Lifshitz 1959). This rate is presented here in vector form,

$$\frac{\mathrm{d}E}{\mathrm{d}t} = - \int \left(\frac{\rho}{2} \boldsymbol{u}^2 + P \right) \boldsymbol{u} \cdot \boldsymbol{n} \, \mathrm{d}S, \qquad (2.13)$$

where $\rho \boldsymbol{u}^2/2 + P$ is referred to as the 'total head' in certain thermodynamic control volume analysis. The surface integral can again be eliminated at the far-field boundary, using the same order of magnitude analysis as was used to eliminate the surface integrals in the impulse equation. By this analysis the integrand terms of (2.13), excluding the pressure term, scale with $\tilde{r}^{-5}$, at the far-field boundaries ($x = x_\infty$ and $r = R_\infty$). Since the pressure at these boundaries is assumed to be stagnation pressure P_∞, a finite constant, the pressure integrand term scales with $\tilde{r}^{-1}$. Therefore, the integrand terms vanish faster than the surface of integration expands to infinity, and the surface integral of (2.13) only needs to be evaluated at the entrance boundary, and defining this surface integral in the axisymmetric coordinate system results in

$$\frac{\mathrm{d}E}{\mathrm{d}t} = \pi \int_0^{R_\infty} \left[\left(\rho u^2 + \rho v^2 + 2P \right) ur \right]_{x=x_0} \mathrm{d}r. \qquad (2.14)$$

Therefore, the kinetic energy of the jet is dependent on both the radial velocity, v, and the pressure at the nozzle exit plane, P, both of which are trivial in truly parallel jet flows.

In order to calculate (2.14) for an arbitrary jet flow entering the control volume, the pressure along the entrance boundary must be determined in terms of the jet velocity profiles. This analysis is presented next.

2.4. *Pressure at the nozzle plane*

Since the starting jet is assumed to be axisymmetric, several simplifying assumptions can be made which aid greatly in determination of the pressure at the entrance plane. The irrotationality of the centreline was utilized by Krueger (2005) who derived a model for nozzle pressure using a potential flow analysis and equating the material surface of the leading vortex ring to a translating flat plate. The pressure model presented here is determined in terms of the velocity potential along the axis of symmetry and a relationship involving the rate of change of jet circulation. One useful feature of this derivation is that it does not require any approximations about
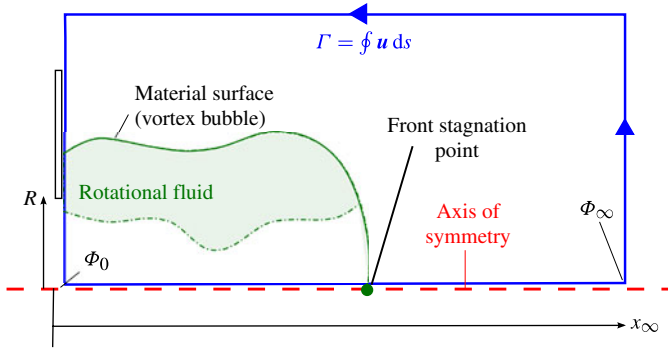
FIGURE 3. (Colour online) The emanating jet flow is depicted along with the line integral used to calculate jet circulation, which is the closed loop. The velocity potential at the entrance boundary and far-field boundary are marked by Φ_0 and Φ_∞, respectively.

the velocity field within the control volume and only requires the knowledge of the velocity profiles at the entrance boundary.

The axis of symmetry is a streamline, given the axisymmetric condition that radial velocity is equal to zero at the centreline. The axis of symmetry is also devoid of vorticity if the axial velocity profile is assumed to be continuous and smooth across the axis. Therefore, the pressure along this axis can be described by the unsteady form of Bernoulli's equation,

$$\frac{\partial \Phi}{\partial t} + \frac{1}{2}\boldsymbol{u}^2 + \frac{P}{\rho} = f(t), \qquad (2.15)$$

where Φ is the velocity potential and $f(t)$ is an arbitrary function which only depends on time. Since the axis of symmetry is irrotational, the velocity potential can be determined from the axial velocity by definition of the potential function, $\nabla\Phi \equiv \boldsymbol{u}$. In cylindrical coordinates the axial velocity becomes $u = \partial\Phi/\partial x$. This flow is illustrated in figure 3. At the far boundary in the axial direction, $x = x_\infty$, the fluid is at stagnation pressure P_∞. Integrating the axial velocity along the centreline we have a relationship between velocity potential at the far boundary, Φ_∞, and the potential at the entrance plane, Φ_0,

$$\Phi_0 = \Phi_\infty - \int_{x_0}^{x_\infty} u \, dx. \qquad (2.16)$$

The velocity along the centreline is not easily determined; however, the line integral of this velocity is contained in the total jet circulation. The circulation is, by definition, the closed-loop line integral of velocity around the axisymmetric plane, which can be separated into sections. Since the line integrals along the far-field boundaries drop to zero, by a similar order of magnitude analysis as that presented in the previous section, the circulation is

$$\Gamma = \oint \boldsymbol{u} \cdot d\boldsymbol{l} = \int_{R_\infty}^{0} v \, dr + \int_{x_0}^{x_\infty} u \, dx. \qquad (2.17)$$

Combining (2.16) and (2.17) gives the potential at the entrance plane as

$$\Phi_0 = \Phi_\infty - \left[\Gamma + \int_0^{R_\infty} v \, \mathrm{d}r\right]. \tag{2.18}$$

Applying Bernoulli's equation at the entrance and far-field boundaries and equating $f(t)$ which has no spacial dependence results in

$$\frac{\partial \Phi_0}{\partial t} + \frac{1}{2}u_0^2 + \frac{P_0}{\rho} = \frac{\partial \Phi_\infty}{\partial t} + \frac{P_\infty}{\rho}, \tag{2.19}$$

where P_0 is the pressure on the centreline at entrance plane. Inserting the derivative of (2.18), and noting that the boundary $r = R_\infty$ remains stationary relates the centreline pressure to circulation and entrance kinematics,

$$P_0 = P_\infty + \rho \frac{\mathrm{d}\Gamma}{\mathrm{d}t} + \rho \int_0^{R_\infty} \frac{\partial v}{\partial t} \, \mathrm{d}r - \frac{\rho}{2}u_0^2. \tag{2.20}$$

Although different methods were used in the derivation, it should be noted that this same equation was derived by Krueger & Gharib (2005, equation (8)). The rate of change of circulation is equal to the flux of vorticity across the nozzle exit plane. Inserting (2.5) into (2.20) allows the pressure on the centreline to be calculated,

$$P_0 = P_\infty + \rho \int_0^{R_\infty} \left(u\frac{\partial v}{\partial x} + \frac{\partial v}{\partial t}\right) \, \mathrm{d}r. \tag{2.21}$$

The pressure along the rest of the entrance plane can be determined by integrating the momentum equation in the radial direction,

$$P(r) = P_0 - \rho \int_0^r \left(u\frac{\partial v}{\partial x} + \frac{\partial v}{\partial t}\right) \, \mathrm{d}\varpi - \frac{\rho}{2}v(r)^2, \tag{2.22}$$

where ϖ is a dummy variable for the radius of integration. Finally combining (2.21) and (2.22) gives the pressure distribution along the entrance plane in terms of surface integrals of jet velocity profiles,

$$P(r) = P_\infty - \frac{\rho}{2}v(r)^2 + \rho \int_r^{R_\infty} \left(u\frac{\partial v}{\partial x} + \frac{\partial v}{\partial t}\right) \, \mathrm{d}\varpi. \tag{2.23}$$

Now the pressure and kinetic energy of any axisymmetric jet flow can be determined as long as the jet kinematics are known at the entrance boundary. Section 6 describes the velocity profiles of jets which are expelled through nozzles to create both parallel starting jet flows and flows with a converging radial velocity. These profiles are then applied to the equations for circulation, impulse, pressure and energy that were just derived, and compared with actual circulation, impulse and energy of jet flows measured experimentally, but first we will discuss the experimental apparatus used to generate these flows in more detail.

3. Vortex/flow generator

The vortex generator used to create the jet flows in this investigation consists of a sealed-off canister submerged in a fluid reservoir. The vortex generator has an internal cavity with a moving plunger to move fluid in or out of the cavity, see figure 4. The plunger is a semi-flexible accordion style bellows which expands axially but maintains
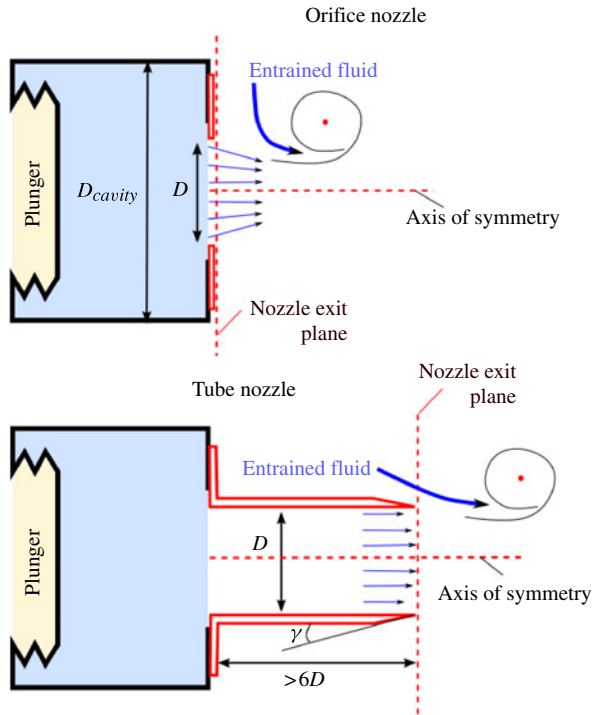
FIGURE 4. (Colour online) Conceptual diagram of the layout of different nozzles used to generate jet flows for this experiment. The nozzle exit plane marked in this figure is considered the entrance plane for the control volume analysis of § 2.

a constant diameter. The expansion is driven by a mechanical system with an ability to create any desired deflection program.

3.1. *Nozzle configurations*

The cavity is attached to both tube and orifice nozzles in order to create both parallel and converging jets. The different nozzle arrangements are illustrated in figure 4. Even though this investigation only tests a limited number of starting flows, the theory presented to model jet circulation, impulse and energy should still be valid for a number of other nozzle configurations, such as diverging jets expelled from a diverging conical nozzle.

3.1.1. *Orifice configuration*

In this configuration the nozzle is simply a flat plate with a central circular orifice. Since the flat plate is located directly on the entrance boundary, the only flow entering the control volume is the fluid passing through the nozzle and all of the fluid which becomes entrained in the primary vortex ring is acquired within the control volume. The orifice nozzle is made out of a sheet of stainless steel, with a thickness less than 1 mm. The orifice nozzle in figure 4 is not drawn to scale and it should be noted that the orifice nozzle thickness is much less than the nozzle diameter (less than 5 % of the diameter), so that the edge can be considered sharp.

3.1.2. *Tube configuration*

The nozzle for this configuration is a long tube connected to the end of the cavity. The tube is sufficiently long, $>6D$, to ensure a parallel flow in the tube prior to ejection. The outside of the tube is tapered at the exit with an angle, γ, as shown in figure 4. The tube nozzles used in this investigation have a taper angle of $\gamma \approx 11°$. With very low γ, there is significant fluid entrainment which takes place at the nozzle exit plane (which is the entrance boundary of the control volume). This means that the volume flux across the entrance boundary will be larger than the volume flux exiting the tube nozzle. The exact extent of this fluid entrainment taking place at the entrance boundary is presented in § 7.1.

Studies which use piston–cylinder-type vortex generators have observed that leading vortex ring formation is closely linked to the jet stroke ratio, which is defined as the ratio of piston stroke length, L, to cylinder diameter, D. The stroke length, L, is slightly ambiguous for flow generators which use a diaphragm or plunger to actuate the flow, since the length of the hypothetical slug of fluid is not necessarily equal to the stroke length of the driving mechanism. Therefore, we define the piston velocity in general to be the average jet axial velocity, $u_p \equiv \Omega/\pi R^2$, where R is the nozzle radius and Ω is the volume flux. The stroke length is then the integral of the piston velocity. The formation time is defined by Gharib *et al.* (1998) as $t^\star = \int_0^t u_p \, d\tau/D$, which is essentially a measure of the time since inception of the flow normalized by the piston velocity and nozzle diameter, and flows with the same stroke ratio will be terminated at the same formation time. Using the vortex generator described here we created both parallel and non-parallel starting jets using nozzles with radii of 1.3 cm (0.5 in) and 0.9 cm (0.36 in) for both nozzle configurations. Since the vortex generator produces all jets with the same volume (33.6 ml), decreasing nozzle diameter is roughly equivalent to increasing the stroke length of a piston–cylinder-style vortex generator. For a nozzle radius of 1.3 cm our generator produces a jet with a stroke ratio $L/D = 2.4$, and a nozzle radius of 0.9 cm produces a jet with a stroke ratio of $L/D = 6.9$.

As the jet formation time increases, the primary vortex ring grows until it becomes saturated and can no longer accept circulation in its current arrangement, and 'pinches off' from the trailing shear flow. Gharib *et al.* (1998) defined the formation number as the formation time corresponding to the final circulation of the primary vortex ring; and additionally showed that parallel starting jets with a variety of piston velocity programs, $u_p(t)$, have a nearly universal formation number (3.6–4.2). Using the smaller radius nozzle, the jet stroke ratio is well above the universal formation number. Therefore, the primary vortex ring will separate from the shear flow long before the jet flow is ended.

3.2. *Velocity program*

Since this investigation is primarily interested in the effect of converging or diverging radial velocity at the entrance boundary, we would like to avoid any variability in jet dynamics due to an accelerating or decelerating piston velocity program. As an approximation to impulsive velocity programs, which are very difficult to create in practice, this investigation has a brief phase of piston velocity acceleration, followed by nearly constant piston velocity for the remainder of pulsation. The experimental trials utilized in this investigation are summarized in table 1, along with characteristic velocity parameters which will be discussed in § 6. In this table the piston velocity, u_p, is averaged over the entire pulsation. The Reynolds number of each jet is also listed, which is calculated as the quotient of total jet circulation and kinematic viscosity, $Re = \Gamma/\nu$, and the DPIV data is used to calculate total circulation after the jet flow

Case	u_p (cm s^{-1})	Nozzle type	Nozzle radius (cm)	$\frac{L}{D}$	b	$k_1^\star$	$k_2^\star$	Re
1	6.7	Tube	1.3	2.4	9.2	0.08	0.33	3046
2	7.5	Tube	0.91	6.9	4.1	0.06	0.07	7879
3	6.8	Orifice	1.3	2.4	10.9	−0.39	1.0	6044
4	7.4	Orifice	0.93	6.8	10.4	−0.45	1.05	10491
5	12.8	Tube	1.3	2.5	10.5	0.09	0.28	4863
6	10.8	Tube	0.91	6.9	4.4	0.06	0.06	10178
7	12.5	Orifice	1.3	2.4	11.1	−0.41	1.01	8454
8	8.7	Orifice	1.3	2.4	11.3	−0.44	1.0	5976
9	10.4	Orifice	0.93	6.8	10.8	−0.44	0.98	11241
10	5.4	Orifice	0.93	6.8	8.2	−0.42	0.97	7205

TABLE 1. Summary of driving conditions for all experimental trials, $k_1^\star$, $k_2^\star$ and b are all parameters corresponding to the resulting jet velocity profiles as will be described in §6. All values which vary with time are taken as the average over the entire pulsation, with the exception of b which is averaged after initial transients have subsided.
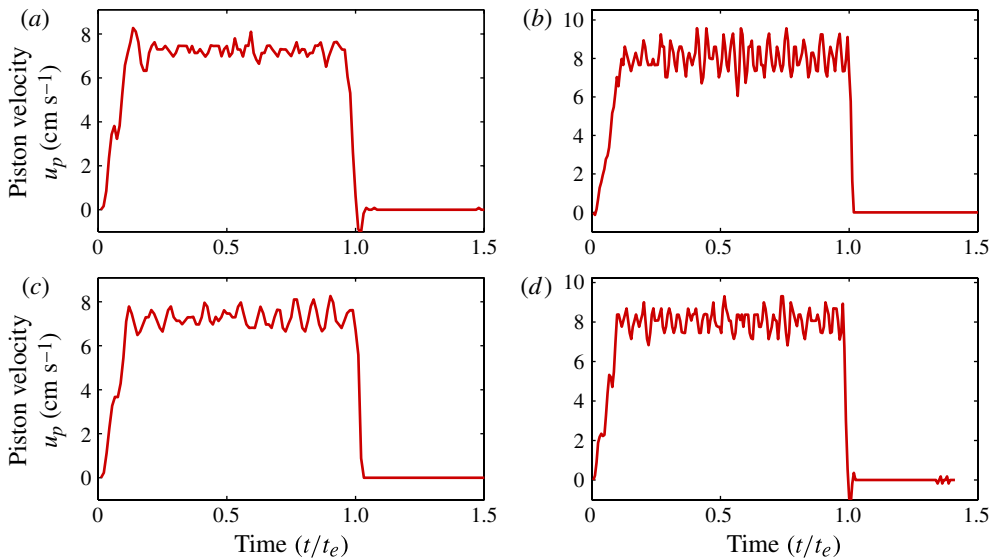

FIGURE 5. (Colour online) Piston velocity programs for several trials, summarized as cases 1–4 in table 1: (*a*) case 1; (*b*) case 2; (*c*) case 3; (*d*) case 4.

has been terminated. The actual piston velocity programs of cases 1–4 are presented in figure 5. The velocity programs are shown for these cases in particular because quantities of these cases will be plotted individually in later figures. Cases 5–10 are not plotted individually, and are mainly used in the velocity profile parameterization, but their velocity programs and bulk flow properties are very similar to cases 1–4. Although the piston velocity is held mainly constant for the duration of pulsation for these cases, there is some small oscillation in piston velocity throughout the entire pulsation associated with vibrations in the mechanical system.
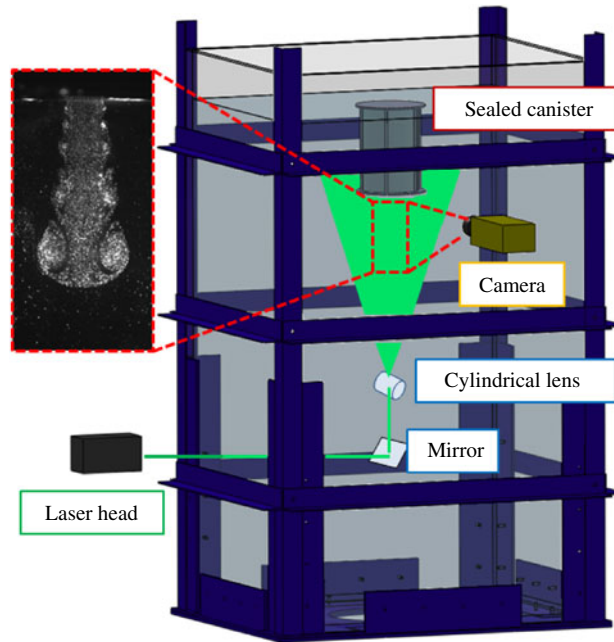
FIGURE 6. (Colour online) Arrangement of the testing tank and flow visualization set-up.

During testing the piston velocity is determined from motor encoder data, assuming that a deflection of the plunger is linearly proportional to the volume displacement. Since the plunger is partially constructed with a flexible rubber which might have load-dependent deformation characteristics, DPIV data was taken of the flow internal to one of the tube nozzles, to validate the volume displacement relationship. This validation is given in appendix A.

4. Experimental set-up

The experimental set-up for this research consists of three primary components whose layout is depicted in figure 6; these are the tank which houses the fluid reservoir, a high-speed camera filming the jet flow, and a data acquisition assembly which sends driving signals to the vortex generator, sends trigger signals to the camera and records motor encoder data. The vortex generator mechanism is sealed within a transparent canister which is submerged fully within the fluid reservoir in the testing tank. A vertical rod runs from the canister to a frame mounting structure keeping the canister stationary.

4.1. *Fluid reservoir*

The water tank, which encompasses the fluid reservoir (control volume of § 2), was designed and fabricated by our group specifically for this investigation, and can be seen in figure 6. It is 2.4 m tall, 1 m by 1.3 m in cross-section and houses 2.65 kl of water. The tank is made out of acrylic to allow for visual access from all angles (including the bottom of the tank) and is supported by an outer steel skeleton. At the top of the tank is a mounting structure which is securely attached to the outer frame. This mounting structure holds the vortex generator in a central position, to avoid wall vortex ring interactions.

4.2. *PIV*

The flow visualization set-up is composed of a high-speed camera and illumination apparatus. As depicted in figure 6, a two-dimensional (2D) cross-section of the flow is illuminated with a laser sheet. The flow is seeded with reflective polyamide particles 50 μm in diameter, with a density of 1.03 g cm^{-3} (manufactured by Dantec Dynamics). The laser sheet is generated by a 1 W solid state 532 nm laser (Aixiz GAM 1000B) expanded through a cylindrical lens within the tank. This results in a laser sheet thickness of ≈1 mm at the nozzle exit plane. The illuminated cross-section of the flow is recorded using a high-speed digital camera, operating at 150–250 fps depending on the piston velocity (and sufficiently short exposure to eliminate streaking). The camera used is a monochrome Phantom v210. This camera has a resolution of 1 MP (1280 × 800 pixels) and a light sensitivity of 6000 ISO, making it suitable for DPIV with the solid-state laser.

5. DPIV data analysis

The high-speed video of the jet flow is analysed using a commercial software, with DPIV algorithms similar to those described in Willert & Gharib (1991) and Raffel, Willert & Kompenhans (1998), to determine a velocity field $\boldsymbol{u} = [v, u]^{\mathrm{T}}$ in the illuminated cross-section of the jet flow. Frames (1280 × 800 pixel resolution), were divided into 32 × 32 pixel interrogation windows (with 50 % overlap). Depending on exact nozzle diameter and optical zoom, the total DPIV velocity field domain ranged from 3.83 × 6.12 diameters to 5.22 × 8.35 diameters, with the long dimension aligned with the axis of symmetry, resulting in relative resolutions in the range 10–12 grid-points per diameter. Strict care was taken to ensure that the laser sheet bisected the flow through the jet axis of symmetry, so that the filmed jet flow corresponds to the axisymmetric flow, as modelled in § 2.

Again, the flow is assumed to be axisymmetric with no swirl. Therefore, the total circulation, hydrodynamic impulse and kinetic energy of the control volume can be calculated from the vorticity and velocity fields (Saffman 1992; Lim & Nickels 1995),

$$\Gamma = \int_{x_0}^{x_\infty} \int_0^{R_\infty} \omega \, \mathrm{d}r \, \mathrm{d}x, \qquad (5.1a)$$

$$I = \rho \pi \int_{x_0}^{x_\infty} \int_0^{R_\infty} \omega r^2 \, \mathrm{d}r \, \mathrm{d}x. \qquad (5.1b)$$

$$E = \rho \pi \int_{x_0}^{x_\infty} \int_0^{R_\infty} \left(u^2 + v^2 \right) r \, \mathrm{d}r \, \mathrm{d}x. \qquad (5.1c)$$

The axisymmetric formulation implies that the velocity/vorticity field is known for a single half-plane extending from the axis of symmetry. The DPIV analysis determines the velocity field for the entire plane which gives two axisymmetric sections π rad out of phase. A sample image of the velocity and vorticity fields determined by this process are shown in figure 7. The axis of symmetry, which separates the two half-planes, is determined in the image as the mid-line between the peak in positive and negative vorticity and is shown as the dashed line in figure 7. In order to determine the axis of symmetry with sub-PIV-window accuracy, the peak locations are interpolated from a small vorticity field surrounding the peak measured value. In general, quantities of interest will be calculated for both half-planes given by DPIV analysis and averaged to give a more accurate value.
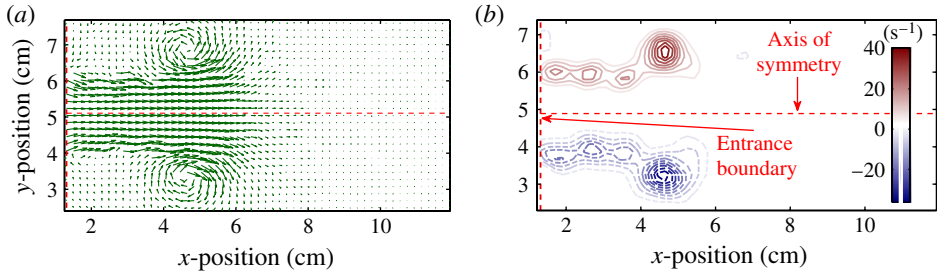
FIGURE 7. (Colour online) Sample image of the velocity field (*a*) and vorticity field (*b*) determined from the DPIV analysis. The axis of symmetry is shown by the dashed red line running horizontal through the centre and the vertical dashed line marks the nozzle exit plane. This sample flow field was generated by a jet ejected from an orifice nozzle with a nozzle radius of 1.3 cm and a piston velocity of ≈ 7 cm s^{-1} (case 3): (*a*) velocity field; (*b*) vorticity field, negative vorticity indicated by dashed isocontours.

These algorithms allow validation of the modelling presented in §2, since the invariants of motion of experimentally generated jet flows can be determined from DPIV data.

6. Velocity profiles at the exit of a family of nozzles

The evolution of circulation, hydrodynamic impulse and kinetic energy of the control volume have been defined in terms of surface integrals of the jet kinematics along the entrance plane in (2.5), (2.9) and (2.14), respectively. The pressure profile along the entrance plane which is needed to calculate the kinetic energy is described by (2.23). The equations are valid for determining the bulk quantities of any inviscid axisymmetric starting jet flow, provided the exact kinematics are known at the source of the flow. The velocity profiles of various starting jets are heavily dependent on the nozzle used to generate the flow. As was mentioned, a starting jet expelled through a long cylindrical nozzle will create a nearly parallel starting jet, whereas converging conical nozzles and orifice nozzles create a starting jet with a converging radial velocity at the entrance boundary. Here we describe jet velocity profiles for starting jets created from both tube and orifice nozzles as observed in previous experiments and measured in this one. We also present multiple approximations to these profiles. Using the approximated jet velocity profiles we calculate the rate of circulation, impulse and energy added to the control volume in terms of characteristic parameters.

6.1. *Axial velocity profile, u*

The axial jet velocity for flows expelled from tube nozzles has been studied extensively. The jet velocity is a dynamic function of both radial position and time, even for programs with constant volume flux. At the onset of the flow the axial jet velocity is nearly uniform with a small peak near the edge due to the influence of the primary vortex ring. This peak is very similar to Richardson's annular effect observed in oscillating pipe flow (Richardson & Tyler 1929) and is seen for jets expelled through both tube nozzles (Didden 1979) and orifice/conical nozzles (Rosenfeld *et al.* 2009). As the piston continues to push out fluid, the boundary layer on the cylinder wall becomes more developed and the jet velocity profile becomes parabolic in tube nozzle flows. Since there is minimal boundary layer development on the orifice nozzle
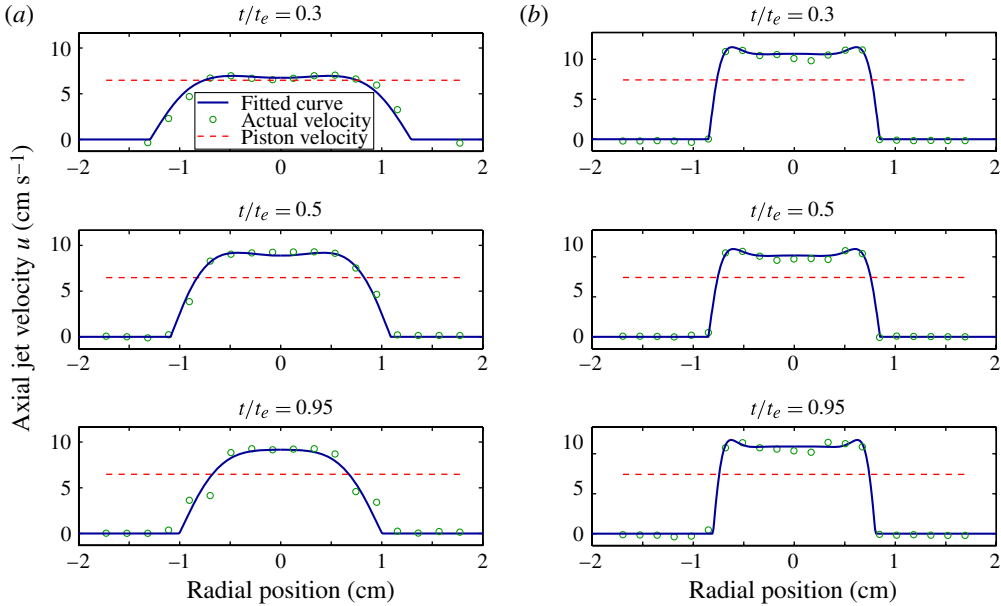
FIGURE 8. (Colour online) Axial velocity profile at the nozzle exit throughout pulsation for a (*a*) tube nozzle (case 2 in table 1) and (*b*) orifice nozzle (case 4 in table 1). The data was fitted to a curve of the form (6.3) described in § 6.1.2.

prior to ejection, the development of a parabolic velocity profile is less pronounced or completely absent if the ratio of the nozzle to cavity diameter is low enough (Rosenfeld *et al.* 2009). For reference the axial velocity profile at the nozzle exit plane (as determined from DPIV analysis) is shown for starting jets ejected from both tube and orifice nozzles in figure 8.

6.1.1. *1D slug model*

The simplest approximation of the jet flow at the nozzle plane is the 1D slug model, which makes the assumption that the jet is ejected with a uniform axial velocity and no radial velocity, $u(r) = u_p$, for $0 \leqslant r < R$. Under these assumptions (2.5), (2.9), (2.23) and (2.14) simplify to the more familiar form,

$$\frac{\mathrm{d}\Gamma_{1D}}{\mathrm{d}t} = \frac{1}{2}u_p(t)^2, \quad \frac{\mathrm{d}I_{1D}}{\mathrm{d}t} = \rho\pi u_p(t)^2 R^2, \quad P_{1D} = P_\infty, \quad \frac{\mathrm{d}E_{1D}}{\mathrm{d}t} = \frac{\rho\pi}{2}u_p(t)^3 R^2. \quad (6.1)$$

This approximation is used frequently for simple calculations, but is only accurate for a very limited range of jet flows. Therefore, we will define a more general axial velocity profile which can be adjusted to fit jet flows found at the outlet of various nozzles at any given time.

6.1.2. *A set of axial velocity profiles parameterized by Bessel functions*

An approximate potential flow solution is derived by Krueger (2005) for the velocity field of jets expelled through tube and orifice nozzles. Both solutions were derived assuming given boundary conditions at the nozzle exit plane. The orifice nozzle solution assumes that the axial velocity is constant over the nozzle area. We would like to avoid this solution since it assumes uniform axial velocity and this investigation characterizes the effect of boundary velocity profiles which deviate from the 1D slug

model. The tube nozzle solution assumes that the velocity potential at the nozzle exit plane is equal to that of a flat plate translating with velocity u_0 at early times, the potential of a steady jet at later times and a mixture of the two at intermediate times, and the weight of each condition is adjusted through a tuning parameter σ. This solution will also be avoided since it violates the no-slip boundary condition at the nozzle edge. Instead, we would like to define a generic set of velocity profiles which are motivated by pipe flow solutions, but allow for a large range of variability.

The velocity profile of flows within a long cylindrical tube has been solved for several different flow configurations. The classical example is the solution for Hagen–Poiseuille flow (fully developed pipe flow). The transient velocity profile in an infinitely long pipe where a uniform, steady pressure gradient is applied at time $t = 0$, was first solved by Szymanski (1932) which is essentially the steady Poiseuille flow with transient terms added which vanish at large times. A solution for oscillating flow within a long cylindrical tube was derived by Sexl (1930), which is summarized by White (2006) as

$$\frac{u}{u_{max}} = \frac{K}{\mathrm{i}\omega}\mathrm{e}^{\mathrm{i}\omega t}\left[1 - \frac{\mathrm{J}_0\left(r\sqrt{\mathrm{i}\omega/\nu}\right)}{\mathrm{J}_0\left(R\sqrt{\mathrm{i}\omega/\nu}\right)}\right], \qquad (6.2)$$

where ω is the frequency of oscillation, K is the amplitude of the pressure gradient oscillation, ν is the kinematic viscosity of the fluid, u_{max} is a velocity scaling term defined, $u_{max} = -(\partial P/\partial x)(R^2/4\mu)$, and J_0 is the zeroth order Bessel function of the first kind. The periodic oscillation is driven by the exponential term, which is only a function of time and the Bessel function terms, dependent on the radial location, provide the velocity profile. As the oscillation frequency increases, the phase lag between the pressure gradient oscillation and velocity oscillation increases, and the velocity profile develops a peak towards the edge of the tube which is known as Richardson's annular effect. The striking similarity between this velocity profile within periodic pipe flows and the velocity profile of starting jets expelled through orifice nozzles (as well as tube nozzle flows at early formation times), suggests that the axial velocity of a starting jet can be approximated by a general form profile involving Bessel functions with complex arguments. Consider the normalized velocity profile with velocity and radius scaling defined $u^\star = u/u_p$ and $r^\star = r/R$, respectively,

$$u^\star(r^\star \leqslant 1) = a\left[1 - \frac{\mathrm{J}_0\left(r^\star b(1-\mathrm{i})\right)}{2\mathrm{J}_0\left(b(1-\mathrm{i})\right)} - \frac{\mathrm{J}_0\left(r^\star b(1+\mathrm{i})\right)}{2\mathrm{J}_0\left(b(1+\mathrm{i})\right)}\right], \quad u^\star(r^\star > 1) = 0, \quad (6.3)$$

where a and b are parameters controlling the shape of the profile. It should be noted that the Bessel function of a complex argument is also complex, so the general profile (6.3) includes a Bessel function term added to its complex conjugate to eliminate the imaginary component. Equation (6.3) is the solution to oscillating pipe flow if the argument parameter is set to $b = \sqrt{\omega/4\nu}$ and the amplitude parameter oscillates with ω.

We denote the volume flux across the entrance plane Ω_{eff}. For actuation methods which have geometries limiting the flow across this plane such as orifice nozzles, the volume flux is just the volume flux supplied by the vortex generator. However, for tube nozzles with small γ, Ω_{eff} is the sum of the supplied flux and the rate at which fluid is entrained at the nozzle exit plane. Maintaining consistency we define effective piston velocity, $u_{eff} = \Omega_{eff}/\pi R_{eff}^2$, and R_{eff} is the radial extent of the jet flow crossing the entrance plane (including entrained fluid). Setting the total volume flux of (6.3) to Ω_{eff}, and using u_{eff} and R_{eff} as the characteristic length and velocity scales restricts
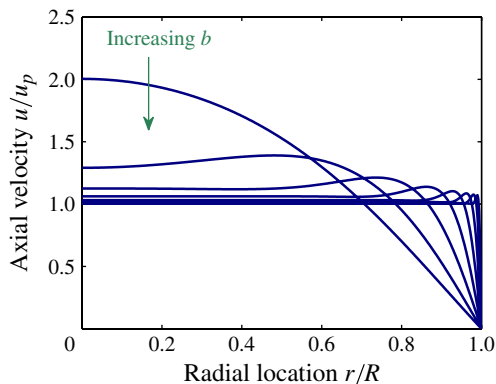
FIGURE 9. (Colour online) Axial velocity profiles at the nozzle plane of the form (6.3), under the constraint (6.4), are shown for several values of b ranging from the limiting value $b = 3.56$ (corresponding to fully developed flow) to $b = 1000$. In general, the profile approaches the hypothetical top hat profile as $b \to \infty$.

the choice of a, and the profile is only parameterized by the term b,

$$a = \left(1 - \frac{1}{b} \left[\frac{\mathrm{J}_1 \left(b(1 - \mathrm{i}) \right)}{(1 - \mathrm{i}) \mathrm{J}_0 \left(b(1 - \mathrm{i}) \right)} + \frac{\mathrm{J}_1 \left(b(1 + \mathrm{i}) \right)}{(1 + \mathrm{i}) \mathrm{J}_0 \left(b(1 + \mathrm{i}) \right)} \right] \right)^{-1}. \tag{6.4}$$

As was noted by White (2006), if the magnitude of the complex argument is very low the velocity profile is a paraboloid approaching the profile of a fully developed pipe flow; whereas, a large argument results in the peak towards $r^\star = 1$ indicative of Richardson's annular effect. Several velocity profiles of the form (6.3) under the constraint (6.4) are shown in figure 9. The argument parameter has a limiting minimum value of $b \approx 3.56$, corresponding to Poiseuille flow. Values of b below this limiting value have an additional inflection point and resemble Gaussian profiles more than parabolic profiles, and as b increases the peak axial velocity decreases and moves towards the nozzle edge, approaching the slug model approximation as $b \to \infty$, which can be observed in figure 9. Therefore, this general axial velocity profile should serve as a decent approximation of many starting jet flows.

As will be shown later, the velocity profile of a jet ejected through an orifice nozzle very quickly reaches a steady distribution that it maintains for the remainder of pulsation. This is because the thinner boundary layer becomes fully developed very quickly and growth of the boundary layer only affects the velocity profile for very short stroke ratio jets. Although this profile will be specific to the exact cavity geometry, a single constant parameter b should be sufficient to characterize the entrance plane kinematics for a given vortex generator and orifice nozzle. Conversely, the velocity profile of jets ejected through tube nozzles varies substantially for a much larger range of stroke ratios due to the more significant boundary layer development. This boundary layer development is dependent on pipe radius, fluid viscosity, and time making an experimental characterization of b undesirable. However, a decent approximation of b for the tube nozzle flow can be calculated by equating the flow to the starting flow in an infinitely long pipe under impulsive initial conditions which is

derived in appendix B and summarized here for convenience:

$$u^\star = \left(1 - r^{\star 2}\right) + \sum_{n=1}^{\infty} \frac{(\lambda_n - 8)J_0\left(\lambda_n r^\star\right)}{\lambda_n^3 J_1\left(\lambda_n\right)} e^{-((\lambda_n^2 - 4\alpha)\nu/R^2)t}. \tag{6.5}$$

In this equation λ_n are the roots of J_0 and α is the magnitude of a transient increase in pressure gradient required to maintain nearly impulsive flow. In order to ensure that the volume flux reaches 95 % of its steady-state value within 0.2 s (which is typical of velocity programs in this experiment, see figure 5) α must be set to 40 for low-stroke-ratio, large-diameter, cases and 20 for high-stroke-ratio, small-diameter, cases. The parameter b is then predicted by fitting the solution to the form (6.3), and will be shown along with the parameter fit to the actual velocity profile later in §7.2.

Since the normalized piston velocity, $u^\star$, is purely a function of b, and is scaled by the piston velocity, evaluating (2.5), (2.9) and (2.14) with an entrance velocity profile defined by (6.3) under the constraint (6.4) will predict circulation, impulse and energy proportional to the 1D slug model,

$$\frac{\mathrm{d}\Gamma_{AP}}{\mathrm{d}t} = \frac{1}{2}u_{eff}^2 f\left(b\right), \tag{6.6a}$$

$$\frac{\mathrm{d}I_{AP}}{\mathrm{d}t} = \rho\pi u_{eff}^2 R_{eff}^2 g\left(b\right), \tag{6.6b}$$

$$\frac{\mathrm{d}E_{AP}}{\mathrm{d}t} = \frac{\rho\pi}{2}u_{eff}^3 R_{eff}^2 h\left(b\right), \tag{6.6c}$$

where

$$f\left(b\right) = \left[b\frac{2C - J_0(b(1+\mathrm{i})) - J_0(b(1-\mathrm{i}))}{2bC - (1+\mathrm{i})A - (1-\mathrm{i})B}\right]^2, \tag{6.6d}$$

$$g\left(b\right) = 2b^2 \frac{3C^2 + \frac{1}{2}A^2 + \frac{1}{2}B^2 + \frac{3(1-\mathrm{i})}{2b\mathrm{i}}CA - \frac{3(1+\mathrm{i})}{2b\mathrm{i}}CB}{[2bC - (1+\mathrm{i})A - (1-\mathrm{i})B]^2}, \tag{6.6e}$$

and

$$A = J_1(b(1-\mathrm{i}))J_0(b(1+\mathrm{i})), \tag{6.6f}$$

$$B = J_1(b(1+\mathrm{i}))J_0(b(1-\mathrm{i})), \tag{6.6g}$$

$$C = J_0(b(1-\mathrm{i}))J_0(b(1+\mathrm{i})). \tag{6.6h}$$

The subscript AP refers to the quantities calculated from the axial velocity parameterization. Here $h(b)$ is not presented in terms of elementary functions, but is shown with respect to the parameter b in figure 10. As can be seen in this figure $h(b)$ can be approximated fairly well by $g(b)$, which should not be surprising given their similar dependence to piston velocity and nozzle radius.

So far the jet velocity characterization at the nozzle plane has only described the axial velocity profile. Next we define a parameterization for the radial velocity profile in a non-parallel starting jets.

6.2. *Radial velocity profile (v)*

At the onset of pulsation the emerging shear tube rapidly rolls into a vortex ring. As a result of the primary vortex ring's close proximity to the nozzle exit plane, the emerging flow from both nozzles experiences an induced velocity in the radial direction. As the vortex ring travels downstream, tube nozzle flows quickly become
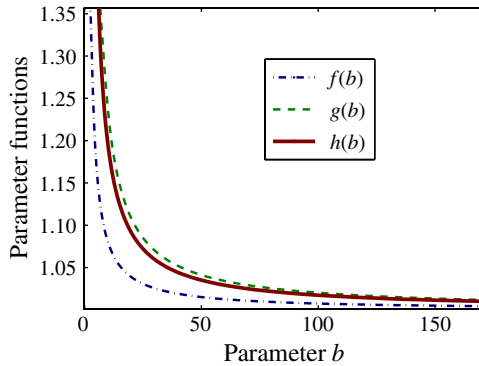
FIGURE 10. (Colour online) Circulation, impulse and energy functions f, g and h are shown with respect to parameter b.
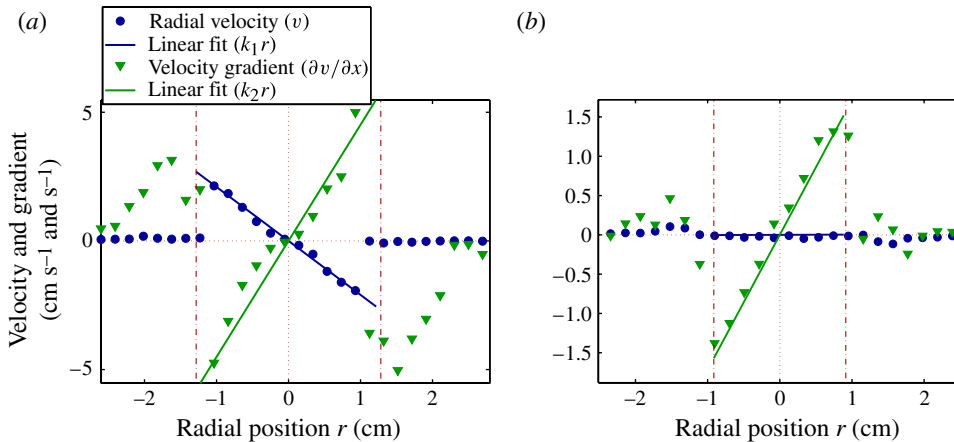

FIGURE 11. (Colour online) Radial velocity and gradient of the radial velocity ($\partial v/\partial x$) as a function of radius, at the exit of both orifice (*a*) and tube (*b*) nozzles. The jets are expelled with a piston velocity of 7 cm s^{-1}. Actual values are shown by markers and a linear fit is shown by the solid line, the nozzle radius for each case is marked by the dashed vertical line. It should be noted that the figures have different velocity scales.

parallel; while the flow emerging from the orifice nozzle maintains a consistent radial velocity throughout pulsation.

6.2.1. *2D jet model*

The simplest radial velocity profile (noting $v(r=0)=0$) is a linear proportionality, $v(r)=k_1 r$ for $0 \leqslant r < R$. In fact, the radial velocity profile at the exit of an orifice nozzle is seen to be approximately linear. Experimental DPIV data of the radial velocity profile at the exit of both tube and orifice nozzles is averaged over the entire pulsation and shown in figure 11. The gradient of the radial velocity in the axial direction, $\partial v/\partial x$, is also averaged over the pulsation and depicted in figure 11. Like the radial velocity, the gradient is assumed to be linear over the same domain, $\partial v/\partial x = k_2 r$, which is a fair approximation. A linear fit to both the radial velocity

and the velocity gradient profiles are also shown in figure 11. The slope of the radial velocity, k_1, has the units of s^{-1}, and the slope of the velocity gradient, k_2, has units cm^{-1} s^{-1}, and both slopes are dependent on the exact nozzle configuration and jetting velocity. Using the piston velocity, u_p, and nozzle radius, R, as characteristic velocity and length scales (same scaling as the axial velocity profile) the dimensionless slope of the radial velocity and velocity gradient are $k_1^\star = k_1 R / u_p$ and $k_2^\star = k_2 R^2 / u_p$. Assuming that the jet has a linear radial velocity profile and a uniform axial velocity the contributions to circulation, impulse, nozzle pressure and energy from the additional terms in (2.5), (2.9), (2.23) and (2.14) are calculated and denoted by the subscript *LR*. Interestingly these contributions have a similar dependence to piston velocity and nozzle radius as the 1D slug model when represented in dimensionless form:

$$\frac{\mathrm{d}\Gamma_{LR}}{\mathrm{d}t} = \frac{1}{2}u_p^2 k_2^\star = k_2^\star \frac{\mathrm{d}\Gamma_{1D}}{\mathrm{d}t}, \tag{6.7a}$$

$$\frac{\mathrm{d}I_{LR}}{\mathrm{d}t} = \frac{\rho\pi}{4}u_p^2 R^2 \left(k_2^\star - k_1^{\star 2}\right) = \frac{k_2^\star - k_1^{\star 2}}{4}\frac{\mathrm{d}I_{1D}}{\mathrm{d}t}, \tag{6.7b}$$

$$P_{LR}(r^\star) = \frac{\rho}{2}u_p^2 \left[k_2^\star - r^{\star 2}\left(k_2^\star + k_1^{\star 2}\right)\right] + \frac{\rho R^2}{2}\frac{\partial k_1}{\partial t}\left(1 - r^{\star 2}\right), \tag{6.7c}$$

$$\frac{\mathrm{d}E_{LR}}{\mathrm{d}t} = \frac{\rho\pi}{4}u_p^3 R^2 \left(k_2^\star + \frac{R^2}{u_p}\frac{\partial k_1}{\partial t}\right) = \frac{1}{2}\left(k_2^\star + \frac{R^2}{u_p}\frac{\partial k_1}{\partial t}\right)\frac{\mathrm{d}E_{1D}}{\mathrm{d}t}. \tag{6.7d}$$

The contributions to bulk flow quantities due to the additional radial velocity terms are calculated assuming a uniform axial velocity profile for simplicity; however, these contributions will be added to the axial velocity parameter model to give the total circulation, impulse and energy. Although the most accurate method would be to use the generic axial profile (6.3) when calculating (6.7), the small increase in accuracy does not justify the increased complexity of the radial contribution terms and equation (6.7) will be used to describe the contributions from non-zero radial velocity terms for all cases. Therefore, the total circulation, impulse and energy of the jet is calculated as the sum of these two contributions, ignoring the term $\partial k_1 / \partial t$ (which is only non-negligible in truly impulsive flows),

$$\frac{\mathrm{d}\Gamma_{2D}}{\mathrm{d}t} = \frac{\mathrm{d}\Gamma_{AP}}{\mathrm{d}t} + \frac{\mathrm{d}\Gamma_{LR}}{\mathrm{d}t} = \frac{\mathrm{d}\Gamma_{1D}}{\mathrm{d}t}\left(f(b) + k_2^\star\right), \tag{6.8a}$$

$$\frac{\mathrm{d}I_{2D}}{\mathrm{d}t} = \frac{\mathrm{d}I_{AP}}{\mathrm{d}t} + \frac{\mathrm{d}I_{LR}}{\mathrm{d}t} = \frac{\mathrm{d}I_{1D}}{\mathrm{d}t}\left(g(b) + \frac{k_2^\star - k_1^{\star 2}}{4}\right), \tag{6.8b}$$

$$\frac{\mathrm{d}E_{2D}}{\mathrm{d}t} = \frac{\mathrm{d}E_{AP}}{\mathrm{d}t} + \frac{\mathrm{d}E_{LR}}{\mathrm{d}t} = \frac{\mathrm{d}E_{1D}}{\mathrm{d}t}\left(h(b) + \frac{k_2^\star}{2}\right). \tag{6.8c}$$

7. Results

The resulting jets for all experimental cases (summarized in table 1) were filmed in cross-section and the video analysed as described in § 5. For every DPIV velocity field the velocity profile of the jet was examined at the nozzle exit plane. The axial velocity profile at this location was fitted to a curve of the form (6.3), using a recursive least-squares algorithm. The radial velocity profile was fit to a line and the slopes k_1 and k_2 recorded over time. The normalized radial slope, $k_1^\star$, normalized radial gradient slope, $k_2^\star$, and axial velocity parameter, b are all presented for the entire pulse duration later in this section and average values are listed in table 1. The parameter b is
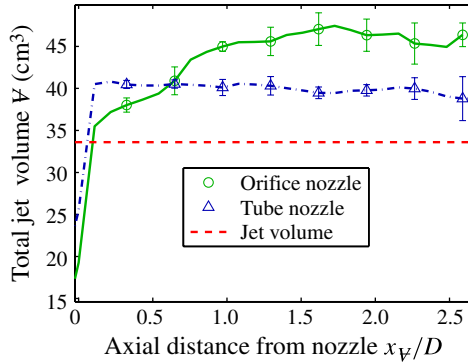
FIGURE 12. (Colour online) Total volume flux in the axial direction as a function of distance from the nozzle plane. Any volume flux above the jet volume (total fluid volume ejected out of the vortex generator) corresponds to entrained fluid. The tube nozzle data is gathered from cases 2 and 6, and the orifice nozzle data from cases 4, 9 and 10, respectively. For all cases the stroke ratio is approximately $L/D \approx 7$, and the error bars indicate standard deviation between cases.

averaged after the initial formation period, because at that time b is very large (close to top hat velocity profile) and tends to misrepresent the data.

7.1. *Volume flux and entrained fluid*

The volume flux, corresponding to jet flow, through any plane orthogonal to the axis of symmetry, at some axial location, x_V, can be determined from the velocity field, $\mathrm{d}V/\mathrm{d}t = \int_0^{R\infty} u(r, x_V) 2\pi r \, \mathrm{d}r$. The total jet volume to pass through this plane is simply, $V = \int_0^{t_+} \int_0^{R\infty} u(r, x_V) 2\pi r \, \mathrm{d}r \, \mathrm{d}t$, where t_+ is some time well after the jet flow is terminated, t_e. We calculated the total jet volume to pass through every plane in a region just downstream of the nozzle exit plane which is presented as a function of axial distance from the nozzle in figure 12. In this figure the curve for the tube nozzle is averaged from cases 2 and 6 (as summarized in table 1), and the curve for the orifice nozzle is averaged from cases 4, 9 and 10.

Also shown in figure 12 is the ejected jet volume or volume of fluid expelled from the vortex generator. It can be seen that the jets expelled from the tube nozzle entrained ≈ 8 ml of fluid right at the nozzle plane. This instantaneous entrainment of fluid can be explained by the fact that the driving flow is expelled out of a long thin cylindrical tube; which allows fluid upstream of the nozzle plane to be drawn into the low pressure roll up (see figure 4). After this initial entrainment the shear tube travels downstream under its own induction velocity without entraining any additional fluid, where it eventually rolls into the primary vortex ring or is left in the trailing wake. This entrainment corresponds to 25 % of the jet volume expelled from the vortex generator, which is similar to entrainment fractions observed by Dabiri & Gharib (2004) and Olcay & Krueger (2008). Dabiri and Gharib measured entrainment fractions around 30–40 % for jets expelled with no counterflow, and Olcay and Krueger observed entrainment fractions from 20 to 45 % depending on the stroke ratio and jet velocity program, showing a large increase in entrainment fraction at very low stroke ratios ($L/D \leqslant 1$). The entrained volume analysis presented here is not meant to augment or verify these results, but rather show that the entrainment takes
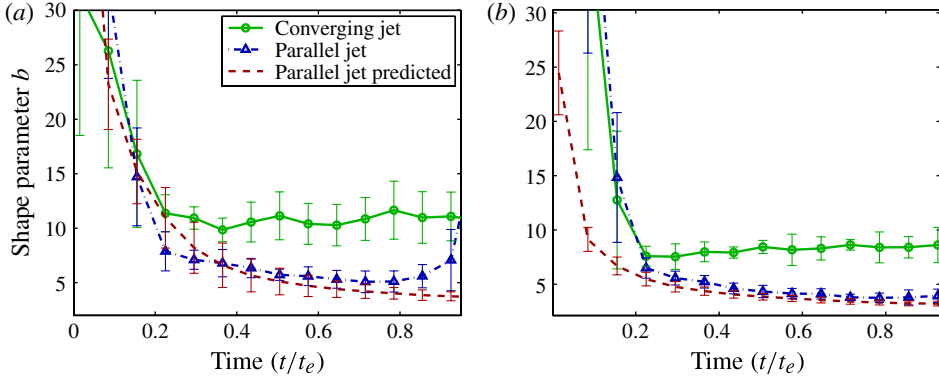
FIGURE 13. (Colour online) Axial velocity profile parameter b versus time for both parallel and converging jets at (*a*) low stroke ratios, $L/D = 2.4$ and (*b*) high stroke ratios, $L/D \approx 7$. The values of b predicted for parallel jets are found solving (6.5) and fitting to the general form (6.3).

place at or around the nozzle exit plane, for tube nozzle flows, which will greatly affect the volume flux at the entrance plane, Ω_{eff}.

The fact that the orifice nozzle forms a physical barrier at the entrance plane means that there is no flow normal to the plane outside of the nozzle radius. Therefore, all entrained fluid must come from the radial direction and the total jet volume to pass through the nozzle exit plane is much closer to that of the ejected jet volume. Set-up limitations prevent the velocity profile from being determined exactly at the nozzle exit plane, and is instead measured a very short distance, ≈ 2 mm, downstream. This is why there is a small amount of initial entrained fluid being measured. However, this measured initial entrainment is very small and the vortex generator flow rate can be used as the volume flux at the nozzle exit plane, Ω_{eff}, without compromising accuracy. Within a short axial distance (less than a diameter) the converging jet has entrained the same volume of fluid as the parallel jet and continues to entrain fluid while contracting until reaching the *vena contracta* plane, at which point the converging jet has entrained 15 ml of fluid, close to 50 % of the ejected jet volume.

7.2. *Jet flow parameters at the nozzle*

7.2.1. *Axial velocity parameter b*

The axial velocity parameterization using Bessel functions (§ 6.1.2) defines the axial velocity profile at the nozzle exit plane, in terms of the parameters u_{eff}, R_{eff}, and b. The volume flux was determined at the nozzle plane (as well the rest of the control volume) as was described in § 7.1, which was used to define the effective volume flux, $\Omega_{eff} = \mathrm{d}\Psi/\mathrm{d}t|_{x=x_0}$; the other two coefficients were determined by fitting the DPIV data at the nozzle exit to the form of (6.3) in a least-squares sense. It should be noted that the residuals in the least-squares algorithm were weighted with the nozzle radius to reflect the larger quantity of fluid corresponding to the velocity value at large radii.

Figure 13(*a*) shows the value of b fitted to the jet velocity profile for both converging and parallel jets with $L/D = 2.4$ corresponding to cases 1, 3, 5, 7 and 8. Also shown in this figure is the value of b predicted by equating the flow to impulsively started flow in a long tube (6.5) as a function of time. It can be seen that the velocity profile of the converging jet acquires a fairly constant value for b very quickly, whereas the jet expelled through the tube nozzle has a slowly decreasing b
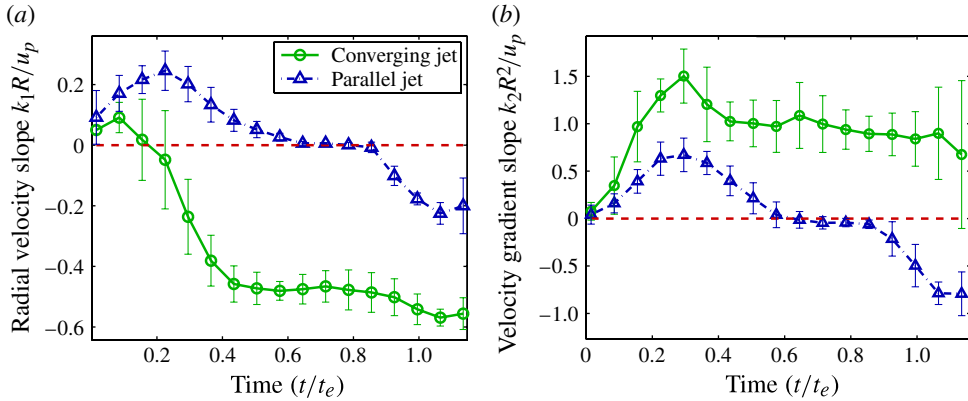
FIGURE 14. (Colour online) The dimensionless slope of (*a*) the radial velocity profile, $k_1^\star$, and (*b*) the gradient of the radial velocity profile, $k_2^\star$, for jets with a stroke ratio of $L/D = 2.4$, expelled through both tube and orifice nozzles. Parallel jets are averaged from cases 1 and 5 and non-parallel jets are averaged from cases 3, 7 and 8.

due to development of the boundary layer. The predicted value of *b* is seen to be a decent approximation of the tube nozzle velocity profile, except at the very end when the development of a stopping vortex influences the profile before the flow has been terminated, as is discussed further in the next section. Figure 13(*b*) shows the fitted and predicted values of *b* for the large stroke ratio converging and parallel jets, corresponding to cases 2, 4, 6, 9 and 10. Similar to the low-stroke-ratio jets the orifice nozzle cases reach a value for *b* which remains relatively constant and the parallel jets have a decreasing value of *b* which is well predicted by the long tube starting flow approximation after the onset of flow where the predicted value is too low, which is likely due to the fact that the impulsive pipe flow conditions are not as valid at the very early stages. Here the final value of *b* drops a bit lower corresponding to a more developed boundary layer at the final time.

7.2.2. *Radial velocity profile*

The radial velocity at the nozzle exit plane was fit to a linear form within the nozzle region using a least-squares algorithm to determine k_1 at every time. The gradient of the radial velocity in the axial direction was determined at the nozzle exit plane using a second-order forward differencing scheme which was also fit to a linear form within the nozzle region to determine k_2. The dimensionless slope of the radial velocity, $k_1^\star$, is shown versus time in figure 14(*a*), for both parallel and converging jets with a low stroke ratio, $L/D = 2.4$. At the initiation of motion the jet flow expands outwards and both jets show a positive slope (diverging radial velocity) corresponding to the initial roll-up of the free shear layer. As the vortex ring moves downstream, the radial velocity of the parallel jet drops to zero until the flow is terminated and the development of a stopping vortex induces a negative radial velocity profile. The slope of the radial velocity profile for the converging jet quickly reaches a negative value (converging radial velocity) which it maintains throughout the rest of the pulsation. Figure 14(*b*) shows the dimensionless slope of the radial velocity gradient, $k_2^\star$. Again the parallel jet radial velocity is due to the roll-up of the leading vortex ring and stopping vortex ring with nearly zero slope in between. The slope of the converging jet radial velocity gradient is larger and persists throughout pulsation as would be
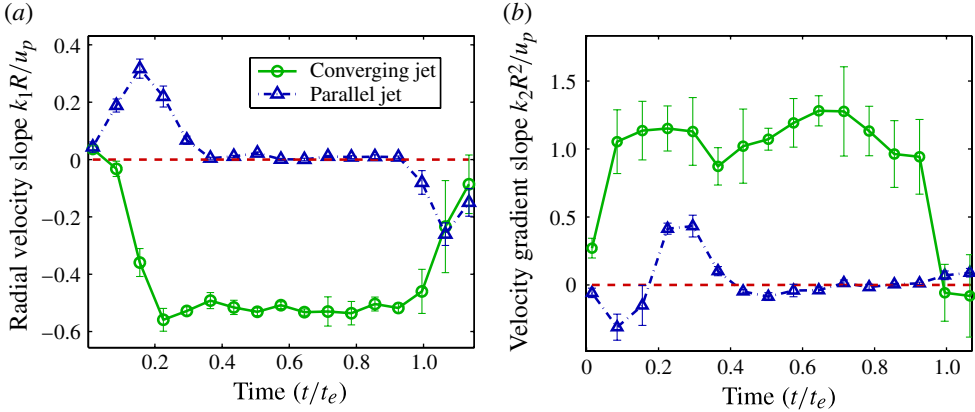
FIGURE 15. (Colour online) The dimensionless slope of (*a*) radial velocity profile, $k_1^\star$, and (*b*) gradient of the radial velocity profile, $k_2^\star$, for jets with a stroke ratio of $L/D \approx 7$, expelled through both tube and orifice nozzles. Parallel jets are averaged from cases 2 and 6 and non-parallel jets are averaged from cases 4, 9 and 10.

expected, but here the primary vortex ring has a more significant presence increasing the slope of $\partial v / \partial x$ in the initial formation period.

The dimensionless slopes $k_1^\star$ and $k_2^\star$ are shown in figure 15 for the jets with a large stroke ratio. The converging jet, averaged from cases 4, 9 and 10, shows the same behaviour as the low-stroke-ratio trials, but the influence of the primary vortex ring is much less noticeable and can be considered negligible. It should be noted here that k_1 and k_2 actually vary significantly between different trials not just because of the different piston velocities, but also because the ratio of nozzle diameter to inner cavity diameter varies between trials (larger stroke ratio corresponding to smaller diameter). Fortunately, the normalization employed to scale these slopes results in a convergence of $k_1^\star$ and $k_2^\star$, not just for trials with different piston velocities, but also for the different nozzle diameters.

The slope of the radial velocity and velocity gradient of the parallel jet at large stroke ratio, cases 2 and 6, also display similar behaviour as the low-stroke-ratio trials, but as would be expected, the jet spends a longer period of time with no induced radial velocity. In addition, the radial velocity gradient of the parallel jets has a negative value for a very short period of time, due to the rapid acceleration of fluid during vortex ring formation. This negative gradient was not observed for the low-stroke-ratio case because the piston velocity acceleration occurred before any significant vortex ring formation.

Here it is interesting to note that nearly the entire jet will end up in the primary vortex ring for the parallel jet expelled through the larger nozzle (low-stroke-ratio) trials, cases 1 and 5. Despite the lack of separation between the vortex ring and the trailing shear flow, figure 14 shows that there is a clear point where the primary vortex no longer induces any appreciable radial velocity at the nozzle exit plane, which is at a formation time of $t^\star \approx 1.2$ and is before the vortex ring separates from the shear flow.

7.3. *Evaluation of jet models*

Now all of the parameters characterizing jet kinematics at the entrance boundary have been determined for the experimental flows. These parameters will be used to predict
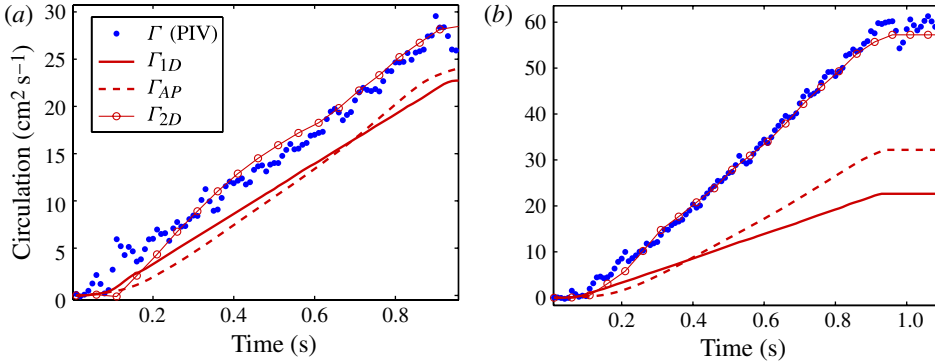
FIGURE 16. (Colour online) Evolution of circulation for (*a*) a parallel jet, case 1, and (*b*) a converging jet, case 3, with a stroke ratio of $L/D = 2.4$ and a jet velocity of ≈ 7 cm s^{-1}.

jet circulation, impulse and energy according to the modelling of §§ 2 and 6, which will be compared to actual circulation, impulse and energy of the jet to validate this modelling.

The circulation, impulse and energy of the control volume were determined from the DPIV vorticity data as described in § 5 and the evolution recorded over time. The slopes of the radial velocity profile and the velocity gradient profile ($k_1^\star$ and $k_2^\star$), as well as the parameters (b and R_{eff}) determined by curve fitting in § 7.2, were used to predict the circulation, impulse and energy according to (6.1), (6.6) and (6.8). The accuracy of all three models is discussed here for each quantity.

7.3.1. *Circulation*

Figure 16 shows the evolution of circulation for both parallel and converging starting jets with a stroke ratio of $L/D = 2.4$ and piston velocity of $u_p \approx 7$ cm s^{-1} (cases 1 and 3). It can be seen from this figure that the total circulation of the jet is well predicted by the 2D model (6.8) for both nozzle configurations.

The circulation of the parallel jet (case 1) is fairly closely approximated by all three models, with the 1D slug model predicting the lowest circulation at the final time when the jet flow is terminated. The rate of circulation added to the system is dependent on the centreline axial velocity, u_0, and not the piston velocity, u_p; therefore, a parabolic velocity profile will have a greater flux of circulation for the same piston velocity. The axial velocity parameter model accurately captures the parabolic axial profile, but still calculates the final circulation too low. Including contributions from vortex ring-induced radial velocity brings the calculated circulation very close to the final jet circulation.

The total circulation of the converging jet just after pulsation is significantly higher than the circulation predicted by the 1D slug model and the axial velocity parameter model. In this configuration the centreline velocity still experiences a slight increase, which causes the axial velocity parameter model to calculate a higher circulation than the 1D slug model, but the effect of the converging radial velocity at the entrance boundary is much more apparent. Including the contribution from the radial terms nearly doubles the computed circulation and captures the actual circulation of the jet. This radial velocity component causes the total circulation of the converging jet to be double the total circulation of the parallel jet (103 % larger), for the same piston velocity and a low stroke ratio, $L/D = 2.4$.
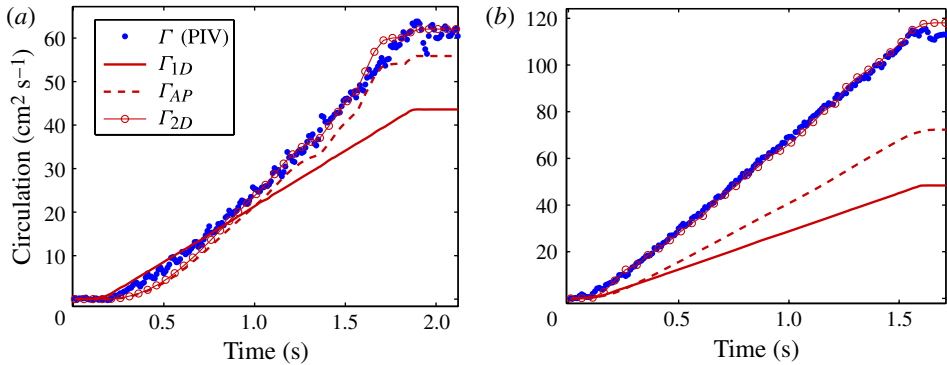
FIGURE 17. (Colour online) Evolution of circulation for (*a*) a parallel jet, case 2, and (*b*) a converging jet, case 4, with a stroke ratio of $L/D \approx 7$ and a jet velocity of ≈ 7 cm s^{-1}.

The circulation of both parallel and converging jets with a larger stroke ratio, $L/D \approx 7$, is shown in figure 17, and again the 2D model circulation comes close to the circulation of both parallel and converging jets. Here the longer formation time and more developed axial velocity profile of the parallel jet produces a large increase in circulation; as is calculated by the axial velocity parameterization. Whereas the effect of the radial velocity component, which exists for a short period of time during initial ring formation, only increases the predicted circulation by a negligible amount. The converging jet experiences less development in the axial velocity profile due to boundary layer growth and the axial velocity parameter model for this case calculates a similar increase over the 1D slug model as the low-stroke-ratio case. The persistent converging radial velocity again nearly doubles the total jet circulation which is captured by the 2D model. In total, the converging jet produces 94 % more circulation than the parallel jet with a stroke ratio $L/D \approx 7$.

7.3.2. *Impulse*

One reason for the deviation of the axial velocity parameter model from the 1D slug model for tube nozzle flows is the change in the effective volume flux, Ω_{eff}, and effective radius, R_{eff}, which are due to entrainment of fluid at the entrance boundary. Interestingly the initial entrained fluid increases the effective volume flux for the parallel jet, but it also increases the effective radius, sometimes to the point where there is a slight decrease in effective piston velocity. This effect can result in a total jet impulse which is lower than that predicted by the 1D slug model as can be seen in figure 18, which shows the total impulse of both parallel and converging jets with a stroke ratio $L/D = 2.4$. This fairly minimal decrease in impulse of the parallel jet is captured by the axial velocity parameter model, and the contribution from the radial velocity terms is negligible for this case. Krueger & Gharib (2003) measured the total impulse imparted by expelling a parallel jet with a stroke ratio of $L/D = 2$, to be 40 % larger than the 'momentum impulse', which is given by the 1D slug model. The discrepancy between those results and impulse measured for parallel jets in this investigation could result from a number of differences in the experimental set-up. The velocity program used here has a very fast acceleration then levels off and remains at a constant value for the rest of the pulsation, as opposed to the velocity programs of Krueger and Gharib which are more triangular than trapezoidal. The slow acceleration might cause the vortex ring to grow close to the nozzle exit for a longer period of
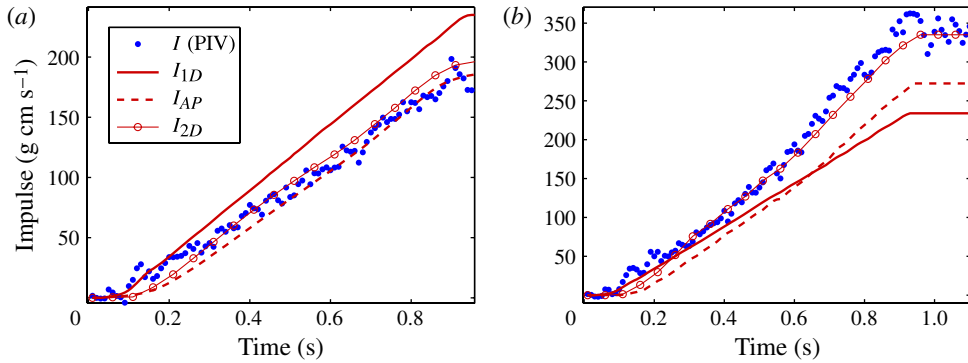
FIGURE 18. (Colour online) Evolution of impulse for (*a*) a parallel jet, case 1, and (*b*) a converging jet, case 3, with a stroke ratio of $L/D = 2.4$ and a jet velocity of ≈ 7 cm s^{-1}.
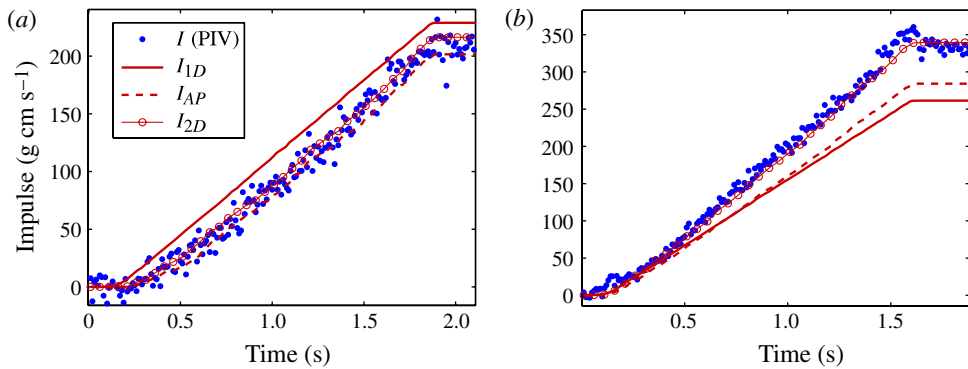

FIGURE 19. (Colour online) Evolution of impulse for (*a*) a parallel jet, case 2, and (*b*) a converging jet, case 4, with a stroke ratio of $L/D \approx 7$ and a jet velocity of ≈ 7 cm s^{-1}.

time and induce a more significant radial velocity on the starting jet, especially since the slope of the radial velocity gradient, $k_2^\star$, was observed in figure 15 to be sensitive to the acceleration during the vortex ring formation stages for tube nozzle flows. In addition, the jets of Krueger and Gharib have a Reynolds number on the order of 20 000, whereas the parallel jet of figure 18(*a*) has a Reynolds number of 3046 and the thinning of the shear layer associated with increased Reynolds number possibly helps to keep the effective radius small.

The axial velocity parameter model shows that the converging jet impulse is increased due to the peak of the axial velocity towards the edge of the nozzle, but the jet impulse is mostly affected by the radial velocity, and again the increase is accurately captured by the 2D model. Overall the converging jet impulse is 73 % higher than the parallel jet for the same piston velocity with a low stroke ratio.

Figure 19 shows the hydrodynamic impulse of both parallel and converging jets with a stroke ratio $L/D \approx 7$. The impulse of the parallel jet is fairly well predicted by the 1D slug model. The effect of the radial velocity induced by the formation of the primary vortex ring is almost non-existent for the parallel jet with a large stroke ratio. The total converging jet impulse is well captured by the 2D model. In total
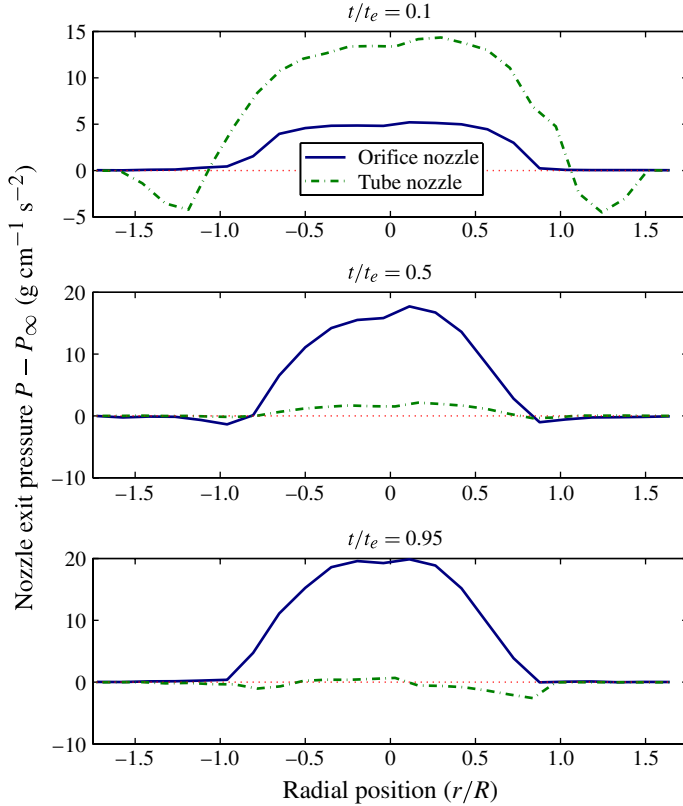
FIGURE 20. (Colour online) Pressure distribution is shown over the nozzle exit area for both tube and orifice nozzles. Both cases are shown for low-stroke-ratio jets with a piston velocity of $\approx 7\ \mathrm{cm\ s^{-1}}$ (cases 1 and 3).

the converging jet has 75 % more impulse than the parallel jet with the same piston velocity and stroke ratio, $L/D \approx 7$. Again the impulse measured for the parallel jet does not acquire the 'pressure impulse' reported by Krueger & Gharib (2003) for a stroke ratio $L/D = 8$; however, it should be noted that at such large stroke ratios the additional thrust attributed to nozzle over-pressure is greatly diminished because of the marginalized influence of the initial vortex ring formation.

7.3.3. *Kinetic energy and nozzle pressure*

The kinetic energy of the jets were determined using the DPIV algorithms and recorded over time. Unfortunately, there is no direct pressure measurement at the nozzle exit plane, so the accuracy of nozzle pressure calculation is difficult to determine. However, the energy model requires knowledge of the pressure at the nozzle (pressure work done at the boundary), so that validation of the kinetic energy indirectly validates the pressure model as well. Even though the pressure distribution was not measured experimentally, it was calculated at the nozzle exit plane from the jet velocity profile according to (2.23). The pressure profile is shown with respect to radius in figure 20. It can be seen in this figure that the initial stages of vortex ring formation induce over-pressure within the nozzle exit area and under-pressure just outside the nozzle radius, for both cases, but the over-pressure on the orifice nozzle is
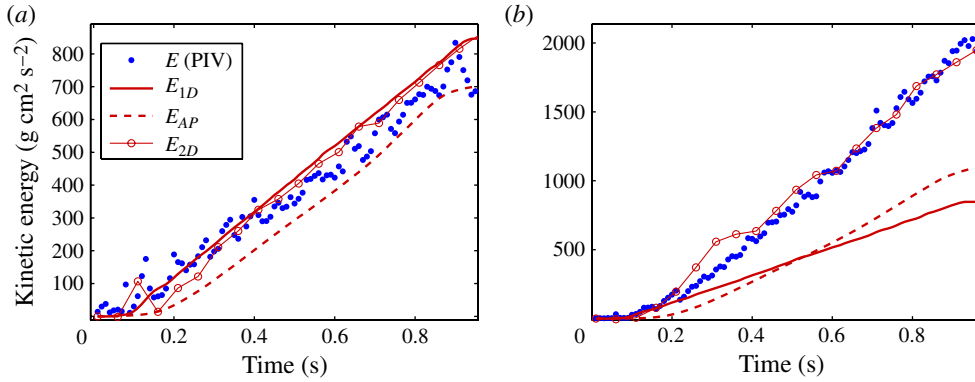
FIGURE 21. (Colour online) Kinetic energy of jets created with a piston velocity of ≈ 7 cm s^{-1} and stroke ratio of $L/D = 2.4$: (*a*) a parallel jet, case 1, and (*b*) a converging jet, case 3.
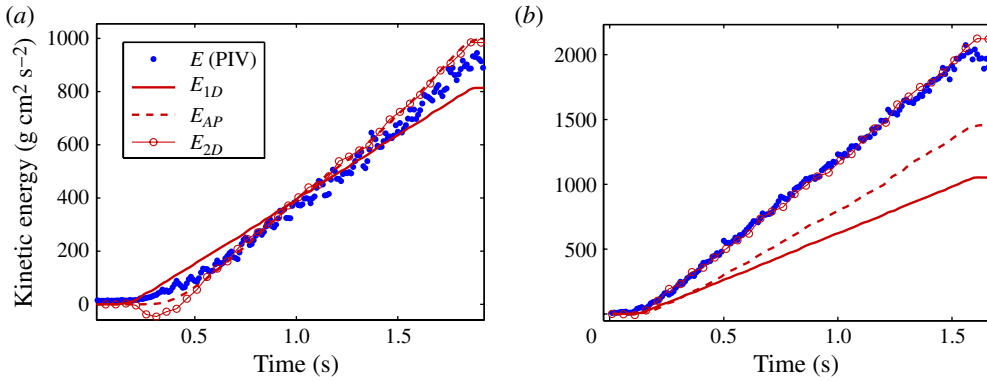

FIGURE 22. (Colour online) Kinetic energy of jets created with a piston velocity of ≈ 7 cm s^{-1} and stroke ratio of $L/D \approx 7$: (*a*) a parallel jet, case 2, and (*b*) a converging jet, case 4.

minimal at the start of motion. After this formation period the converging jet maintains over-pressure at the nozzle exit area but the parallel jet drops to stagnation pressure.

The kinetic energy of both parallel and converging starting jets, expelled with low stroke ratios, $L/D = 2.4$, and equivalent piston velocities $u_p \approx 7$ cm s^{-1} are shown in figure 21. While the parallel jet energy is well captured by the 1D slug model, the converging jet has a much larger kinetic energy. Some of the additional energy is due to a peak in axial velocity towards the nozzle edge; however, a much larger portion of the increased energy is due to the increased pressure at the centreline required to support the radial velocity gradient. The 2D model provides a very close approximation to the actual kinetic energy of the jet. Overall the converging jet has a kinetic energy more than double (135 %) the parallel jet.

For the jets with large stroke ratio, $L/D \approx 7$, again all three models provide a decent approximation of the parallel jet energy, as can be seen in figure 22, and the 2D model accurately computes kinetic energy of the converging jet. Overall the converging jet contains 105 % more kinetic energy than the parallel jet, for large stroke ratios.

8. Conclusion

There are several real-world flows which involve non-parallel starting jets, but analysis has been largely focused on parallel starting jets; and specifically those created by a piston–cylinder vortex generator. It was demonstrated here that the 1D slug model, which is traditionally used to model circulation, impulse and energy of starting jets, drastically under-predicts these quantities if the incoming flow has a converging radial velocity and it is predicted that the 1D slug model will over-predict the quantities if there is a diverging radial velocity. In addition, the 1D slug model provides a poor prediction of the circulation of parallel jets and provides a poor prediction of the impulse of parallel jets at low stroke ratios, where the leading vortex ring and boundary layer development have a strong influence on the incoming jet flow, as has been observed previously.

These model deficiencies were addressed by Krueger & Gharib (2005) by including contributions from over-pressure; whereas, this paper derives a new model to predict circulation, impulse and energy of starting jets which specifically accounts for a radial velocity at the source of the jet flow. This model only requires the knowledge of jet kinematics at the entrance boundary of any axisymmetric control volume. This is a powerful tool for modelling jet flows and can even be extended to continuous jets by changing the treatment of far-field boundaries, as will be examined in future publications. We also presented generic axial and radial velocity profiles which can be used to parameterize a wide variety of experimental jet flows, and the jet circulation, impulse and energy were then derived in terms of the velocity profile parameters.

One obvious application of modelling starting jet impulse comes in the design of pulsatile jet thrusters for underwater vehicle maneuvering. This analysis allows the total jet impulse to be optimized for any given flow constraint in terms of the limited number of jet flow parameters. Although not specifically addressed here, future studies will identify exactly how the velocity parameters, b, $k_1^\star$ and $k_2^\star$, can be adjusted by nozzle geometry and piston velocity programs. This will reduce the problem to designing a device which creates optimal velocity parameters, rather than optimizing the thrust of the device through the slow process of testing all the various nozzle configurations until an optimum is found. Another similar application is the design of more effective synthetic jet actuators.

Both parallel and converging starting jets were created experimentally by ejecting fluid through a set of tube and orifice nozzles, and the velocity fields of these jets were captured using DPIV techniques. The DPIV data was used to parameterize the velocity profiles at the exit of these nozzles, as well as to validate the circulation, impulse and energy models. The velocity profiles of parallel jets expelled through a tube nozzle and subsequently circulation, impulse and energy of the jet are highly sensitive to the formation of the primary vortex ring as indicated by the large variation in dynamics between high and low stroke ratios. Whereas, the orifice nozzle used to create a converging jet resulted in a more uniform velocity profile throughout pulsation for all stroke ratio. The radial velocity at the entrance boundary has a drastic effect on the circulation, impulse and energy of the starting jet. The converging jet was observed to have as much as 100 % more circulation and energy, and 75 % more impulse than the parallel jet with the same mass flux and nozzle diameter, and this increase was very well captured by the new jet model.

Ignoring the radial velocity will create an under-specified model for circulation, impulse, and energy (meaning that a model scaled only by characteristic axial velocity will predict the same quantities for parallel and converging jets with the same piston velocity), which will result in significant scatter in reported experimental data for jet
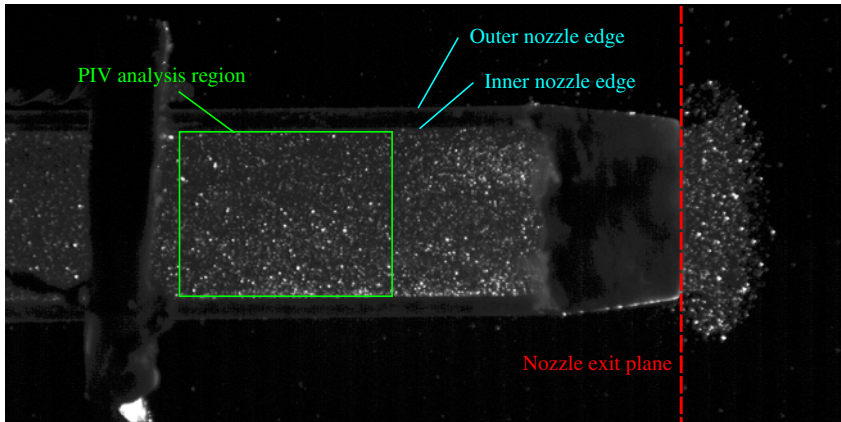
FIGURE 23. (Colour online) A single frame depicting the flow visualization used to calibrate piston velocity. Seeding particles are illuminated by a laser sheet entering from the nozzle opening.

circulation, impulse and energy with a given characteristic axial velocity. Rather than focusing on corrections to an overly simplified model which are geometry specific, we believe a more fundamental understanding comes from incorporating the radial velocity in the normalizations and then identifying how the nozzle geometry affects these quantities. This could have a profound effect on analysis of synthetic jet actuators which have a wide variety of publications focusing on the effect of the specific orifice geometry.

Acknowledgements

Appendix A. Piston velocity validation

The piston velocity, u_p, is determined from motor encoder velocity, assuming that the plunger has a linear correspondence between deflection and volume displacement. The displaced volume was measured at several plunger deflections to test this relationship. However, this testing used static volume measurement techniques and further validation was needed to ensure that this relationship is preserved during high-speed operation, especially considering that the plunger is constructed with a flexible rubber which might have load-dependent deformation characteristics.

Fortunately, one of the tube nozzles is constructed out of clear acrylic which allowed visual access to the internal flow. A sample image of the clear tube nozzle with illuminated internal flow is depicted in figure 23.

A typical driving signal was sent to the thruster (nearly impulsive program described in § 3.2). The internal tube flow was filmed and processed using the commercial DPIV algorithms (see § 5). The velocity profile across the nozzle area was determined at multiple locations. Although the nozzle itself is a cylindrical plastic tube, the optical density of acrylic is close enough to water that the optical distortion will be negligible. The velocity profile across the nozzle was also observed to be nearly uniform except
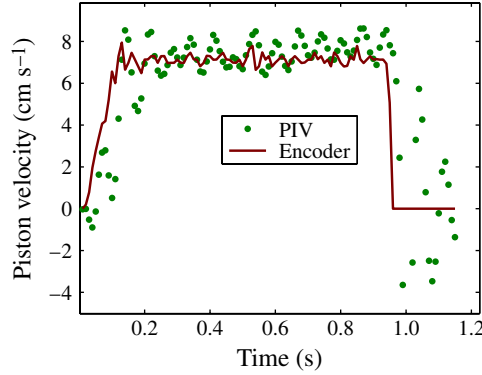
FIGURE 24. (Colour online) Piston velocity is shown versus time determined form DPIV and motor encoder data.

at the nozzle surface accounting for boundary layer development. The volume flux, Ω, was calculated by integrating the DPIV velocity profile over the nozzle area,

$$\Omega = 2\pi \int_0^R ur \, \mathrm{d}r. \tag{A 1}$$

The piston velocity is determined from the volume flux in the usual way, $u_p = \Omega/\pi R^2$. The piston velocity was also determined from the motor encoder data for the same trial run. The piston velocity determined from each method is plotted as a function of time in figure 24.

For the majority of the pulsation the piston velocity determined from DPIV matches the piston velocity determined by the encoder with the exception of the end of pulsation where the sudden termination of plunger motion results in some oscillation associated with elastic vibrations in the plunger surface.

Appendix B. Analytic pipe flow solutions for impulsive startup

Consider the flow in an infinitely long pipe, such that the radial velocity, v, vanishes and the governing dynamics of the flow can be described by the Navier–Stokes equation in the axial direction,

$$\frac{\partial u}{\partial t} = -\frac{1}{\rho}\frac{\partial P}{\partial x} + \nu \left[\frac{\partial^2 u}{\partial r^2} + \frac{1}{r}\frac{\partial u}{\partial r}\right], \tag{B 1}$$

or in non-dimensional terms with normalized variables $u^\star = u/u_m$ and $r^\star = r/R$,

$$\frac{\partial u^\star}{\partial t} = -\frac{1}{u_m\rho}\frac{\partial P}{\partial x} + \frac{\nu}{R^2}\left[\frac{\partial^2 u^\star}{\partial r^{\star 2}} + \frac{1}{r^\star}\frac{\partial u^\star}{\partial r^\star}\right]. \tag{B 2}$$

Szymanski (1932) solved this flow analytically assuming a constant pressure gradient, enforcing the no-slip boundary condition at the edge of the pipe $u^\star(t, 1) = 0$, and imposing the initial condition that the flow starts at rest $u^\star(0, r^\star) = 0$. These conditions resulted in the analytical solution,

$$u^\star = \left(1 - r^{\star 2}\right) - \sum_{n=1}^{\infty} \frac{8\mathrm{J}_0\left(\lambda_n r^\star\right)}{\lambda_n^3 \mathrm{J}_1\left(\lambda_n\right)} \mathrm{e}^{-\lambda_n^2 \nu t/R^2}, \tag{B 3}$$

and the velocity scaling is related to the pressure gradient by $u_m = -(\partial P/\partial x)(R^2/4\mu)$. This solution provides an axial velocity profile within the pipe which over time accelerates under the constant pressure gradient and slowly develops a boundary layer on the edge of the pipe, becoming the steady Hagen–Poiseuille flow at large time values. Unfortunately, this flow is not exactly representative of the flow inside the tube nozzle for nearly impulsive velocity programs. For a truly impulsive flow the volume flux through the pipe reaches a steady value at the onset of motion, and this is realized by a pressure gradient which starts out very large and settles upon a constant value as the flow becomes fully developed.

In order to more closely capture this transient behaviour we provide a similar analytical solution with two changes. First it is assumed that the pressure gradient is equal to the sum of a constant and an additional term which diminishes at the same rate as the transients in the flow profile and secondly the initial condition is imposed that at time $t = 0$, the flow starts out with uniform distribution, $u^{\star}(0, r^{\star}) = (1 - H(r^{\star} - 1))/2$, where H is the heaviside function. Although this initial condition is discontinuous it satisfies the no-slip condition and the velocity profile will become continuous immediately after this initial time. If we assume the velocity profile at any time is equal to the steady Poiseuille solution added to the transient terms, $u^{\star} = 1 - r^{\star} + u_1^{\star}(t)u_2^{\star}(r^{\star})$, and assume the pressure gradient transients are proportional to the velocity transients, $\partial P/\partial x = k\left[1 + \alpha u_1^{\star}(t)u_2^{\star}(r^{\star})\right]$, and substitute back into the governing equation (B 3) then the constant pressure gradient terms cancel with spacial derivatives of the steady velocity profile resulting in the same velocity scaling $u_m = -kR^2/4\mu$. The governing equation can then be separated into differential equations of time and radius, both equal to the separation constant, $-\sigma^2$, and the general form of the transients is

$$u_1^{\star}(t)u_2^{\star}(r^{\star}) = Ce^{-\sigma^2 t}J_0(\lambda r^{\star}), \qquad (B\,4)$$

where λ is related to the separation constant, $\sigma^2 = (\lambda^2 - 4\alpha)\nu/R^2$. In order to satisfy the no-slip boundary condition λ must be set to one of the infinite zeros of J_0 denoted λ_n. Imposing the new boundary condition and utilizing the orthogonality of Bessel functions allows the coefficient C_n corresponding to each zero λ_n to be determined,

$$C_n = \frac{\lambda_n^2 - 8}{\lambda_n^3 J_1(\lambda_n)}. \qquad (B\,5)$$

Therefore, the starting flow in an infinitely long pipe under the impulsive initial conditions is

$$u^{\star} = \left(1 - r^{\star 2}\right) + \sum_{n=1}^{\infty} \frac{(\lambda_n - 8)J_0\left(\lambda_n r^{\star}\right)}{\lambda_n^3 J_1\left(\lambda_n\right)} e^{-((\lambda_n^2 - 4\alpha)\nu/R^2)t}. \qquad (B\,6)$$

Setting $\alpha = 0$ produces the velocity profiles in a pipe with a constant pressure gradient and the impulsive initial condition. These velocity profiles are shown over time in figure 25(*a*), which shows that the velocity profile is the uniform 1D slug model profile at time $t = 0$ and becomes nearly fully developed by $t = 10$ s. The average velocity, $\bar{u}$, is easily calculated for this flow as the total volume flux over area, and is shown for this case over the first 5 s of pulsation in figure 25(*b*). It can be seen that at the onset of flow the average velocity is equal to one, corresponding to the impulsive piston velocity as is specified by the initial condition. But the constant pressure gradient is insufficient to maintain this volume flux, which immediately drops and does not return to the impulsive piston velocity until the flow reaches steady state.
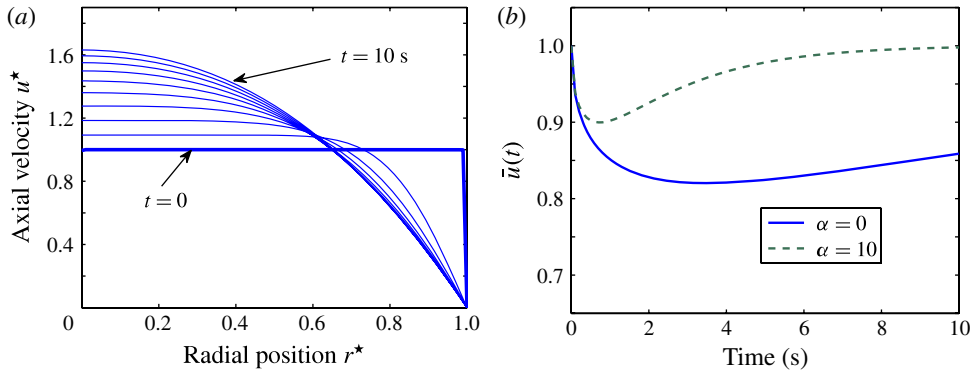
FIGURE 25. (Colour online) The analytical solution to velocity profiles of an impulsively started pipe flow are shown in (*a*) where the parameter α is set to zero. The resulting average velocity at these times are shown for this case in (*b*) as well as the case where $\alpha = 10$.

By increasing the value of α we are essentially increasing the magnitude of the pressure gradient during the transient stages to maintain the impulsive piston velocity. It can be seen in figure 25(*b*) that a larger α ($\alpha = 10$) lessens the drop in volume flux during the transient stages and the increase in pressure gradient during these stages can also be seen to accelerate the boundary layer development. Therefore, the parameter α can be tuned so that the volume flux of the analytical solution comes very close to the volume flux of the nearly impulsive starting flow. If this parameter is tuned correctly, then the analytical solution will provide the velocity profile within the tube nozzle throughout the pulsation. This solution is not valid at the exit plane (or entrance) of the tube nozzle where the spiralling free shear layer induces a radial velocity and axial velocity gradient, $\partial u/\partial x$, contradicting the pipe flow governing equation (B 1). However, the infinite pipe solution does correctly identify the level of boundary layer development giving a reasonable prediction of the axial velocity parameter, *b*, for tube nozzle flows as validated in § 7.2.

REFERENCES

ANDERSON, E. J. & GROSENBAUGH, M. A. 2005 Jet flow in steadily swimming adult squid. *J. Exp. Biol.* **208**, 1125–1146.

BARTOL, I. K., KRUEGER, P. S., STEWART, W. J. & THOMPSON, J. T. 2009 Hydrodynamics of pulsed jetting in juvenile and adult brief squid *Lolliguncula brevis*: evidence of multiple jet 'modes' and their implications for propulsive efficiency. *J. Exp. Biol.* 1189–1903, doi:10.1093/icb/icn043.

BARTOL, I. K., KRUEGER, P. S., THOMPSON, J. T. & STEWART, W. J. 2008 Swimming dynamics and propulsive efficiency of squids throughout ontogeny. *Integr. Compar. Biol.* **48** (6), 1–14.

CANTWELL, B. J. 1986 Viscous starting jets. *J. Fluid Mech.* **173**, 159–189.

DABIRI, J. O. & GHARIB, M. 2004 Fluid entrainment by isolated vortex rings. *J. Fluid Mech.* **511** (4), 311–331.

DABIRI, J. O., COLIN, S. P., KATIJA, K. & COSTELLO, J. H. 2010 A wake based correlate of swimming performance and foraging behaviour in seven co-occurring jellyfish species. *J. Exp. Biol.* **213**, 1217–1275.

DIDDEN, N. 1979 On the formation of vortex rings: rolling-up and production of circulation. *Z. Angew. Mech. Phys.* **30**, 101–116.

GHARIB, M., RAMBOD, E., KHERADVAR, A., SAHN, D. J. & DABIRI, J. O. 2006 Optimal vortex formation as an index of cardiac health. *Proc. Natl Acad. Sci. U.S.A.* **103** (16), 6305–6308.

GHARIB, M., RAMBOD, E. & SHARIFF, K. 1998 A universal time scale for vortex ring formation. *J. Fluid Mech.* **360**, 121–140.

GLEZER, A. 1988 The formation of vortex rings. *Phys. Fluids* **12**, 3532–3542.

HALLER, G. & YUAN, G. 2000 Lagrangian coherent structures and mixing in two-dimensional turbulence. *Physica* D **147**, 352–370.

HOLMAN, R., UTTURKAR, Y., MITTAL, R., SMITH, B. L. & CATTAFESTA, L. 2005 Formation criterion for synthetic jets. *AIAA J.* **43** (10), 2110–2116.

KRIEG, M. & MOHSENI, K. 2008 Thrust characterization of pulsatile vortex ring generators for locomotion of underwater robots. *IEEE J. Ocean. Engng* **33** (2), 123–132.

KRUEGER, P. S. 2005 An over-pressure correction to the slug model for vortex ring circulation. *J. Fluid Mech.* **545**, 427–443.

KRUEGER, P. S. 2008 Circulation and trajectories of vortex rings formed from tube and orifice openings. *Physica* D **237**, 2218–2222.

KRUEGER, P. S. & GHARIB, M. 2003 The significance of vortex ring formation to the impulse and thrust of a starting jet. *Phys. Fluids* **15** (5), 1271–1281.

KRUEGER, P. S. & GHARIB, M. 2005 Thrust augmentation and vortex ring evolution in a fully pulsed jet. *AIAA J.* **43** (4), 792–801.

LAMB, H. 1945 *Hydrodynamics*. Dover.

LANDAU, L. D. & LIFSHITZ, E. M. 1959 Fluid mechanics. In *Ideal Fluids (Energy Flux)*, pp. 9–10. Butterworth-Heinemann, chap. 1.6.

LIM, T. T. & NICKELS, T. B. 1995 Vortex rings. In *Fluid Vortices* (ed. S. I. Green). Kluwer.

LIPINSKI, D. & MOHSENI, K. 2009a Flow structures and fluid transport for the hydromedusa *Sarsia tubulosa*. *AIAA paper* 2009-3974. *19th AIAA Computational Fluid Dynamics Conference, San Antonio, Texas*. Curran Associates Inc.

LIPINSKI, D. & MOHSENI, K. 2009b Flow structures and fluid transport for the hydromedusae *Sarsia tubulosa* and *Aequorea victoria*. *J. Exp. Biol.* **212**, 2436–2447.

MOHSENI, K. 2006 Pulsatile vortex generators for low-speed maneuvering of small underwater vehicles. *Ocean Engng* **33** (16), 2209–2223.

MOHSENI, K. & GHARIB, M. 1998 A model for universal time scale of vortex ring formation. *Phys. Fluids* **10** (10), 2436–2438.

MOHSENI, K., RAN, H. & COLONIUS, T. 2001 Numerical experiments on vortex ring formation. *J. Fluid Mech.* **430**, 267–282.

NITSCHE, M. & KRASNY, R. 1994 A numerical study of vortex ring formation at the edge of a circular tube. *J. Fluid Mech.* **276**, 139–161.

OLCAY, A. B. & KRUEGER, P. S. 2008 Measurement of ambient fluid entrainment during laminar vortex ring formation. *Exp. Fluids* **44** (2), 235–247.

PULLIN, D. I. 1979 Vortex ring formation in tube and orifice openings. *Phys. Fluids* **22**, 401–403.

PULLIN, D. I. 1978 The large-scale structure of unsteady self-similar rolled-up vortex sheets. *J. Fluid Mech.* **88** (3), 401–430.

PULLIN, D. I. & PHILLIPS, W. R. C. 1981 On a generalization of Kaden's problem. *J. Fluid Mech.* **104**, 45–53.

RAFFEL, M., WILLERT, C. E. & KOMPENHANS, J. 1998 *Particle Image Velocimetry*. Springer.

RAJU, R., MITTAL, R., GALLAS, Q. & CATTAFESTA, L. 2005 Scaling of vorticity flux and entrance length effects in zero-net mass-flux devices. In *AIAA 35th Fluid Dynamics Conference and Exhibit. Toronto, Ontario*. AIAA.

RICHARDSON, E. G. & TYLER, E. 1929 The transverse velocity gradients near the mouth of a pipe in which an alternating or continuous flow of air is established. *Proc. Phys. Soc. Lond.* **42**, 1–15.

ROSENFELD, M., KATIJA, K. & DABIRI, J. O. 2009 Circulation generation and vortex ring formation by conic nozzles. *J. Fluids Engng* **131**, 091204.

ROSENFELD, M., RAMBOD, E. & GHARIB, M. 1998 Circulation and formation number of laminar vortex rings. *J. Fluid Mech.* **376**, 297–318.

SAFFMAN, P. G. 1978 The number of waves on unstable vortex rings. *J. Fluid Mech.* **84** (4), 625–639.

SAFFMAN, P. G. 1992 *Vortex Dynamics*. Cambridge University Press.

SAHIN, M. & MOHSENI, K. 2008 The numerical simulation of flow patterns generated by the hydromedusa *Aequorea victoria* using an arbitrary Lagrangian–Eulerian formulation. *AIAA paper* 2008-3715. *38th AIAA Fluid Dynamics Conference and Exhibit, Seattle, OR*. Curran Associates Inc.

SAHIN, M. & MOHSENI, K. 2009 An arbitrary Lagrangian–Eulerian formulation for the numerical simulation of flow patterns generated by the hydromedusa *Aequorea victoria*. *J. Comp. Phys.* **228**, 4588–4605.

SAHIN, M., MOHSENI, K. & COLINS, S. 2009 The numerical comparison of flow patterns and propulsive performances for the hydromedusae *Sarsia tubulosa* and *Aequorea victoria*. *J. Exp. Biol.* **212**, 2656–2667.

SEXL, T. 1930 Uber den von E.G. Righardson entdeckten 'Annulareffekt'. *Z. Phys.* **61**, 349–362.

SHADDEN, S. C., LEKIEN, F. & MARSDEN, J. E. 2005 Definition and properties of Lagrangian coherent structures from finite time Lyapunov exponents in two-dimensional aperiodic flows. *Physica* D **212**, 271–304.

SHARIFF, K. & LEONARD, A. 1992 Vortex rings. *Annu. Rev. Fluid Mech.* **34**, 235–279.

SZYMANSKI, F. 1932 Quelques solutions exactes des équations de l'hydrodynamiquede fluide visqueux dans le cas d'un tube cylindrique. *J. Math. Pures Appl.* **11** (9), 67–107.

WHITE, F. M. 2006 *Viscous Fluid Flow*, 3rd edn. McGraw-Hill.

WILLERT, C. E. & GHARIB, M. 1991 Digital particle image velocimetry. *Exp. Fluids* **10**, 181–193.